Long-lasting synaptic regulation of dopamine neurons by astrocytes in the Ventral Tegmental Area

Linda Requie
CNR Padova
Marta Gómez-Gonzalo
CNR Padova
Francesca Managò
Istituto Italiano di Tecnologia https://orcid.org/0000-0003-3663-6193
Mauro Congiu
Neuroscience Institute, Section of Cagliari, National Research Council , Cagliari
Marcello Melone
Università Politecnica delle Marche, and Center for Neurobiology of Aging, INRCA IRCCS
Angela Chiavegato
Dept. Biomedical Science, University of Padova
Arianna Arianna
Università Politecnica delle Marche
Giada Pacinelli
Genetics of Cognition laboratory, Neuroscience area, Istituto Italiano di Tecnologia (IIT)
Marsicano Giovanni
University of Bordeaux, and Interdisciplinary Institute for Neuroscience, CNRS,
Francesco Papaleo
Genetics of Cognition Laboratory, Neuroscience area, Istituto Italiano di Tecnologia, via Morego, 30, 16163 Genova https://orcid.org/0000-0002-6326-0657
Anna Muntoni
Neuroscience Institute, Cagliari, National Research Council
Fiorenzo Conti
Università Politecnica delle Marche https://orcid.org/0000-0001-5853-1566
Giorgio Carmignoto (✉ giorgio.carmignoto@bio.unipd.it)
Neuroscience Institute, Section of Padova, National Research Council (CNR) and Università degli Studi di Padova https://orcid.org/0000-0003-3063-6774

Article

Keywords: Ventral Tegmental Area (VTA), dopamine neurons, synaptic regulation, Astrocytes

Posted Date: March 23rd, 2021

DOI: https://doi.org/10.21203/rs.3.rs-301561/v1

Long-lasting synaptic regulation of dopamine neurons by astrocytes in the Ventral Tegmental Area

Requie, Linda Maria[1&]; Gómez-Gonzalo, Marta[1&*]; Managò, Francesca[2]; Congiu, Mauro[3]; Melone, Marcello[4]; Chiavegato, Angela[1]; Pugliese, Arianna[4]; Pacinelli, Giada[2]; Marsicano, Giovanni[5]; Papaleo, Francesco[2]; Muntoni, Anna Lisa[3]; Conti, Fiorenzo[4]; Carmignoto, Giorgio[1*]

[1]Neuroscience Institute, Section of Padova, National Research Council (CNR) and Department of Biomedical Sciences, Università degli Studi di Padova, Padova, Italy

[2]Genetics of Cognition laboratory, Neuroscience area, Istituto Italiano di Tecnologia (IIT), Genova, Italy

[3]Neuroscience Institute, Section of Cagliari, National Research Council (CNR), Cagliari, Italy

[4]Department of Experimental and Clinical Medicine (Section of Neuroscience & Cell Biology), Università Politecnica delle Marche, and Center for Neurobiology of Aging, INRCA IRCCS, Ancona, Italy

[5]University of Bordeaux, and Interdisciplinary Institute for Neuroscience, CNRS, Bordeaux, France

[&] Equal contribution

* Corresponding authors

ABSTRACT

The plasticity of glutamatergic transmission in the Ventral Tegmental Area (VTA) represents a fundamental mechanism in the modulation of dopamine neuron burst firing and the phasic dopamine release at VTA target regions. These processes encode basic behavioral responses, including locomotor activity, learning and motivated-behaviors. Here we describe a hitherto unidentified mechanism of long-lasting potentiation of glutamatergic synapses on DA neurons. We found that VTA astrocytes respond to dopamine neuron bursts with Ca^{2+} elevations that require activation of endocannabinoid CB1 and dopamine D2 receptors colocalized at the same astrocytic process. Astrocytes, in turn, release glutamate that, through presynaptic metabotropic glutamate receptor activation coupled with neuronal nitric oxide production, induces long-lasting potentiation of excitatory synapses on adjacent dopamine neurons. Consistent with this finding, selective activation of VTA astrocytes increases dopamine neuron bursts *in vivo* and induces locomotor hyperactivity. Astrocytes play, therefore, a key role in the modulation of VTA dopamine neuron activity.

INTRODUCTION

Dopamine (DA) neurons in the Ventral Tegmental Area (VTA) regulate a wide array of physiological functions including locomotor activity, attention, motivation and reward-based learning[1–3]. A fundamental step in these DA-dependent functions is the transition in the spiking activity of VTA DA neurons from tonic, low frequency firing at rest, to high frequency bursts that modulate the action of DA by determining the synaptic phasic release of DA at VTA target areas such as nucleus accumbens (NAc), medial prefrontal cortex, hippocampus, and amygdala[4–7]. This transition and the bursting activity of DA neurons are under crucial control of glutamatergic afferent inputs to the VTA originating from various brain regions[4,7,8]. Importantly, the enduring changes in the strength of these glutamatergic synapses exert profound effects on DA neurons regulating their burst firing mode and the

release of dopamine at target regions[1,9]. The plasticity of these glutamatergic synapses represents, therefore, a key mechanism in the modulation of DA transmission and DA-dependent behaviors. While extensive studies highlighted the role of neuronal signals in the synaptic plasticity of VTA circuits[1,10], the role of astrocytes has been poorly investigated.

A recent study reported that optogenetic stimulation of channelrhodopsin-expressing VTA astrocytes alters glutamate transport, favoring DA neuron inhibition and avoidance behavior[11]. However, this type of stimulation depolarizes astrocytes, leading to a significant increase in extracellular K^+ and a subsequent neuronal excitation[12]. Whether astrocytes are functionally recruited to the VTA circuitry by neuronal signals and influence the plasticity of glutamatergic synaptic transmission to VTA DA neurons remains totally unexplored.

Astrocytes are active components of brain circuits. Besides their support and metabolic functions, they respond with Ca^{2+} elevations to neurotransmitters and, in turn, release gliotransmitters that regulate synaptic transmission and plasticity[13–15]. Astrocytes are similarly activated by local signals, such as endocannabinoids (eCBs), released by neurons at somatodendritic levels. In various brain areas, including the VTA, eCBs act as retrograde signals that induce depression of synaptic neurotransmitter release upon presynaptic type-1 cannabinoid receptor (CB1R) activation[16,17]. Studies in hippocampus and dorsal striatum revealed that eCBs also target astrocytic CB1Rs evoking Ca^{2+} elevations and glutamate release that potentiates distant excitatory synapses[18–20]. Whether this lateral potentiation of synaptic transmission is also operative in the VTA is unknown.

Using *ex vivo* and *in vivo* approaches, we investigated whether eCBs released by bursting discharges of VTA DA neurons[21] induce a potentiation of glutamatergic transmission to nearby DA neurons and whether this action is mediated by astrocytes. Because VTA DA neurons, beside eCBs, release DA at somatodendritic levels[22], we investigated whether DA is also involved in DA neuron-to-astrocyte signalling. Finally, we evaluated the functional consequences of a specific activation of astrocytes *in vivo* at the

level of both VTA DA neuron firing and locomotor activity. Our results unveil a reciprocal functional signaling between DA neurons and astrocytes in VTA circuits.

RESULTS

Bursting activity of individual VTA DA neurons induces long-lasting potentiation of glutamatergic transmission in adjacent DA neurons. We investigated whether the bursting activity in individual DA neurons evokes lateral potentiation of glutamatergic synaptic transmission[18]. In VTA slices of postnatal day (P)14-17 female mice, we recorded from pairs of neurons exhibiting the typical features of DA neurons (Fig. 1a and Extended Data Fig. 1a-d). In one neuron of the pair, we monitored excitatory post-synaptic currents (EPSCs) evoked by low frequency stimulation of the rostral glutamatergic afferents. To the second neuron, located 70-120 µm apart, we imposed through intracellular current pulses the burst firing mode that characterizes *in vivo* DA neuron activity (bursts of five action potentials at 20 Hz, 2 Hz interburst frequency, 5 min duration; Extended Data Fig. 1e)[23–25]. Following this bursting activity, EPSC amplitude from the first DA neuron was significantly increased and this potentiation was maintained for at least 45 min (Fig. 1b and 1d). The long-lasting potentiation was not observed in age-matched male mice, in which EPSC amplitude was only transiently increased 3 min after bursts (Fig. 1b and 1d). We defined these two forms of lateral synaptic plasticity as burst-induced long- and short-term potentiation (bLTP and bSTP, respectively). Evaluation of the paired-pulse ratio (PPR) in female mice revealed a significant PPR reduction at 30 and 45 minutes after bursts, suggesting a presynaptic mechanism in bLTP generation (Fig. 1c). In contrast, the bSTP in male mice occurred without PPR changes (Fig. 1c). Importantly, the induction of a tonic-like discharge that mimics DA neuron activity at resting conditions (2 Hz action potential frequency for 5 minutes, Extended Data Fig. 1e), failed to modify evoked EPSCs in adjacent

100 DA neurons at any time point tested (Fig. 1d), indicating that bLTP and bSTP are strictly
101 dependent on DA neuron bursting activity.
102
103 **Generation of bLTP requires Ca^{2+} elevations in astrocytes.** We focused our study on
104 bLTP generation mechanism and asked whether astrocytes are involved. We performed
105 experiments in type-2 inositol 1,4,5-trisphosphate receptor knock-out ($IP_3R2^{-/-}$) female mice
106 in which G-protein coupled-mediated astrocyte Ca^{2+} elevations are largely impaired[19,26,27].
107 In VTA slices from these mice, DA neuron bursts evoked transient, but not long-lasting
108 potentiation of synaptic transmission (Fig. 1d), suggesting that bLTP induction depends on
109 IP_3R2-mediated astrocytic Ca^{2+} elevations induced by signals generated by the DA neuron.
110 This hypothesis was directly tested in VTA slices from wild type (wt) and $IP_3R2^{-/-}$ mice loaded
111 with the Ca^{2+} fluorescent indicator Fluo-4 and the specific astrocytic marker SR101. To
112 monitor Ca^{2+} signals from astrocytes in proximity of soma and dendrites, through a patch
113 pipette we filled DA neurons with the fluorescence tracer neurobiotin (Fig. 1e). We observed
114 that the sustained bursting activity of the DA neuron evoked in astrocytes of female, but not
115 male mice, Ca^{2+} elevations that lasted for at least 25 min (Fig. 1f-h). Furthermore, DA neuron
116 bursts failed to evoke Ca^{2+} elevations in astrocytes of $IP_3R2^{-/-}$ female mice (Fig.1h). Overall,
117 these data suggest that astrocyte IP_3R2-mediated Ca^{2+} elevations are required for bLTP
118 generation.
119
120 **Generation of bLTP requires eCB and DA signalling to astrocytes, presynaptic**
121 **mGluR1 activation and nitric oxide release from DA neurons.** To gain further insights
122 into the molecular mechanism of bLTP generation, we investigated whether CB1 and/or DA
123 receptors (Rs), activated by eCBs and/or DA locally released by VTA DA neurons, are
124 involved. We found that applications of either the CB1R antagonist AM251 (2 - 4 µM) or the
125 D2-type receptor antagonist eticlopride (1 µM) prevented bLTP (but not bSTP), whereas the

126 D1-type receptor antagonist SCH-23390 hydrochloride (10 µM) was ineffective (Fig. 2a). We
127 also evaluated the role of the glutamatergic N-methyl-D-Aspartate receptor (NMDAR), which
128 is a fundamental element in the plasticity of glutamatergic synaptic transmission in different
129 brain regions[28], including the VTA[10]. We found that in the presence of the NMDAR
130 antagonist D-AP5 (50 µM), bLTP was unchanged (Fig. 2a), indicating that NMDAR is not
131 involved in bLTP. We then hypothesized an involvement of type 1 metabotropic glutamate
132 receptor (mGluR1) activation, as previously observed for astrocyte-mediated synaptic
133 plasticity in hippocampal[18,19] and striatal circuitries[20]. We found that bLTP was abolished in
134 the presence of the mGluR1 receptor antagonist LY-367385 (100 µM; Fig. 2a). Then, we
135 investigated whether nitric oxide (NO), which contributes to long-term synaptic plasticity in
136 other brain circuits[19,29], is also involved. We found that blocking NO synthesis in the bursting
137 DA neuron using an NO synthase inhibitor (L-NAME)-containing patch pipette (100 µM),
138 abolished bLTP (Fig. 2a). However, a transient EPSC potentiation, that was absent in the
139 presence of the other antagonists which block bLTP (Extended Data Fig. 2a), was observed
140 6 min after DA neuron bursts, suggesting that NO release by DA neurons contributes to the
141 sustained phase of bLTP.

142 We asked whether CB1 and D2R activation, which is required for bLTP generation,
143 is also required for DA neuron burst-induced astrocytic Ca^{2+} elevations. We found that the
144 astrocyte Ca^{2+} response to DA neuron bursts was abolished in the presence of either AM251
145 or eticlopride (Fig. 2b). We next asked whether mGluR1 activation, which is required for
146 bLTP generation, is mediated by astrocytic glutamate. In such a case, the mGluR1
147 antagonist LY-367385 should not block the astrocyte Ca^{2+} response to DA neuron bursts.
148 As expected, the Ca^{2+} response of astrocytes was unaffected by LY-367385 (Fig. 2b).
149 Therefore, mGluR1 activation plays a crucial role in bLTP generation downstream of
150 astrocyte Ca^{2+} signals. Finally, we found that after blocking NO synthesis, DA neuron bursts
151 evoked in astrocytes only a transient Ca^{2+} response (Fig. 2b and Extended Data Fig. 2b),

indicating that NO release by DA neurons contributes to astrocyte Ca^{2+} signal dynamics, as previously reported[30].

In support of the role of astrocytic CB1 and D2-type receptors in bLTP generation, pre-embedding electron microscope (EM) experiments showed that, besides neurons (Extended Data Fig. 3a, Table 1), astrocytes express CB1 and D2-type receptors (D2, D3 and D4R, Fig. 2c, Extended Data Fig. 3b, Table 1 and 2). According to our post-embedding quantitative EM analysis of CB1/D2R immunogold double-labelled astrocytic processes, CB1 and D2Rs colocalize at perisynaptic processes at variable distances (Fig. 2d, e, mean distance: 532.2 ± 49.7 nm), indicating that the same astrocyte can sense both eCBs and DA. Pre-embedding EM analysis also revealed that the mGluR1β isoform is expressed at axon terminals making asymmetric synaptic contacts (Fig. 2c; Extended Data Fig. 3c, Table 2 and 3), consistent with a presynaptic mechanism of bLTP, as suggested by PPR reduction.

Taking all these results together, we propose that bLTP in the VTA circuitry of female mice is evoked by the following sequence of events (Fig. 2f). Firstly, DA neuron bursting activity induces the somatodendritic release of eCBs, DA and NO; secondly, activation of CB1 and D2Rs in astrocytes triggers IP_3R2-dependent Ca^{2+} elevations, modulated by neuronal NO, and a subsequent glutamate release; thirdly, presynaptic mGluR1 activation by astrocytic glutamate, possibly coupled with NO actions on neurons, induces a sustained increase in glutamate release probability leading to bLTP of excitatory transmission onto adjacent DA neurons.

Differential expression of DA, CB1 and mGluR1 receptors in the VTA of young male and female mice. The bLTP was absent in the VTA of young male mice where astrocytes failed to response with Ca^{2+} elevations to DA neuron burst. We hypothesized that the lack of astrocyte Ca^{2+} responses is due to absence or lower levels of CB1 and/or D2Rs in male with respect to female mice. Our pre-embedding EM experiments showed that astrocytes

178 from male mice express CB1, D2, D3 and D4Rs (Fig. 3a and Extended Data Fig. 3a, d).
179 Quantitative evaluation revealed, however, that the expression of CB1 and D2Rs is higher
180 in astrocytic processes of female than male mice ($P < 0.0001$ and $P = 0.033$, respectively;
181 Fig. 3a and Table 2), whereas that of D3Rs is higher in male than female mice ($P < 0.0001$,
182 Extended Data Fig. 3d and Table 2). Furthermore, the percentage of axon terminals
183 expressing mGluR1β in female mice is twice that observed in male mice ($P = 0.016$; Fig. 3a,
184 Extended Data Fig. 3c and Table 2). Therefore, the lack of bLTP in male mice is likely due
185 to a defective astrocyte Ca^{2+} response to DA neuron signalling caused by reduced
186 expression of CB1Rs and different pattern and density of D2/D3Rs in the astrocytic
187 membrane, coupled to mGluR1β reduction which affects the ability of astrocytic glutamate
188 to regulate release probability at glutamatergic axon terminals.
189
190 **Selective chemogenetic activation of astrocytes rescues bLTP in young male mice.** If
191 the lack of bLTP in male mice is due, at least in part, to a lack of astrocyte Ca^{2+} responses
192 to DA neuron bursts, we expect bLTP to be rescued by stimulating astrocyte Ca^{2+} elevations.
193 As a specific stimulus, we used chemogenetic activation of Gq protein-coupled designer
194 receptor exclusively activated by designer drugs (DREADDs, hM3D(Gq)) that were
195 selectively expressed in astrocytes (Fig. 3b, c and Extended Data Fig. 4). In VTA slices from
196 mice that express both DREADDs and GCaMP6f in VTA astrocytes, we observed that bath
197 perfusion with the hM3D(Gq) agonist clozapine N-oxide (CNO, 10 μM) evoked transient
198 Ca^{2+} elevations in hM3D(Gq)-expressing astrocytes (Fig. 3d). In agreement with this
199 transient astrocyte response, parallel experiments performed in the presence of the CB1
200 and D2R antagonists, AM251 and eticlopride, revealed that CNO evoked in male mice
201 expressing hM3Dq in astrocytes, but not in non-injected control mice, a short-lasting
202 potentiation of the excitatory transmission (Fig. 3e), which became a bLTP lasting at least
203 30 min after coupling CNO with DA neuron burst firing (Fig. 3f). These results further suggest

that NO is required for bLTP generation. Given that these experiments were performed in the presence of CB1 and D2R antagonists, these results further support that bLTP generation depends on astrocytic rather than neuronal CB1 and D2Rs.

Astrocytes induce bLTP in the VTA of both female and male adult mice. We next investigated whether the astrocyte-mediated bLTP observed in young mice is also present in young adulthood. We found that in VTA slices from adolescent/adult mice (P30-70, to simplify hereafter adult mice), DA neuron bursts evoked in adjacent DA neurons a bLTP that was maintained for at least 30 min after bursts (Fig. 4a). In contrast to data obtained from young mice, the bLTP in adult mice was observed in both female and male (Fig. 4a). The presence of bLTP in adult male mice could be due to a developmentally regulated expression of CB1, D2 and/or mGluR1β receptors. Quantitative analysis from pre-embedded material of adult male mice showed that the levels of CB1Rs at astrocytic processes and mGluR1β at glutamatergic terminals are, indeed, higher in adult compared to young male mice, while the levels of D2Rs are comparable (Fig. 4b, Table 4). In agreement with the presence of bLTP in both female and male adult mice, quantitative evaluation of mGluR1β, CB1 and D2 receptor expression revealed comparable levels in these mice (Fig. 4b, Extended Data Fig. 5, Table 4). Together with data presented in figure 3f, these results suggest that the absence of bLTP in young male mice is mainly due to CB1R low expression in astrocytic membranes.

The mechanism of bLTP generation in adult mice is similar to that in young female mice, because it was abolished by specific D2, CB1 or mGluR1 receptor antagonists (Extended Data Fig. 6). To further confirm the role played by astrocytic D2 and CB1Rs, we injected the AAV9/2-hGFAP-mCherry_iCre-WPRE-hGHp into the VTA of male mice carrying a “floxed” version of either the D2 or the CB1R genes, to express the Cre recombinase in VTA astrocytes (Fig. 4c). Immunohistochemical experiments showed that

the great majority of mCherry-Cre-immuno positive cells were also GFAP-positive and only a very few mCherry-Cre-immunopositive cells were NeuN-positive (Fig. 4d, Extended Data Fig. 7a, b). As a control, we injected the same AAV vector in wt male mice. We found that bLTP was abolished when the Cre recombinase was expressed in astrocytes containing the D2 or CB1R floxed gene, whereas it could still be evoked when the recombinase was expressed in wt astrocytes (Fig. 4e; see also specific comments on Discussion). Finally, as in young female mice, bLTP in adult male mice was abolished when the NO synthase inhibitor L-NAME was included in the patch pipette (Extended Data Fig. 6), and only a reduced transient potentation lasting no more than 6 min (EPSC amplitude (%) t_{6min} = 112.7 ± 4.4, p = 0.028, n = 7) was observed. Altogether, these data indicate that the astrocyte-mediated bLTP observed in young female mice is preserved in older female mice and is also present in adult male mice with similar cellular and molecular mechanisms.

bLTP is abolished in adult IP3R2$^{-/-}$ mice expressing a plasmatic Ca^{2+} pump in astrocytes. To further explore the role of astrocyte Ca^{2+} signals in bLTP during adulthood, we performed DA neuron-paired recording experiments from VTA slices of adult $IP_3R2^{-/-}$ female and male mice. In both groups, the amplitude of evoked EPSCs showed an increase at 30 min after DA neuron bursts that was not statistically significant (Extended Data Fig. 8). However, after pooling results obtained from both female and male $IP_3R2^{-/-}$ mice together, we observed a statistically significant potentiation of the excitatory transmission at 30 min (Fig. 4g). Consistently, after pooling results obtained from female and male mice together as wt or $IP_3R2^{-/-}$ groups, the percentage of experiments showing bLTP was different ($p < 0.05$, Chi square test, 85.7 % female/male wt mice, n = 14, vs 44.4 % female/male $IP_3R2^{-/-}$ mice, n = 18). These results suggest that the deletion of IP_3R2 has a lower impact on astrocyte Ca^{2+} signal dynamics in adult than young mice and additional experimental tools affecting Ca^{2+} signalling are needed to impair the Ca^{2+} dependent astrocytic actions in adult

mice. To validate this idea, we expressed in astrocytes from $IP_3R2^{-/-}$ mice the plasma membrane Ca^{2+} pump isoform hPMCA2w/b that significantly reduced Ca^{2+} signals in these cells[31] (Fig. 4f and Extended Data Fig. 7c, d). We found that bLTP generation was fully impaired both in female and male $IP_3R2^{-/-}$ mice that expressed hPMCA2w/b in VTA astrocytes (Fig. 4g and Extended Data Fig. 8). Therefore, Ca^{2+} signaling is crucial for bLTP generation also in adult mice, but the impairment of the IP_3R2-mediated signalling in these mice is not sufficient to block astrocyte Ca^{2+}-dependent actions.

In vivo **activation of VTA astrocytes favors DA neuron bursts and induces long-lasting motor hyperactivity.** Glutamatergic synapses in the VTA circuitry modulate the firing activity of DA neurons and their potentiation, mainly mediated by NMDARs, enhances the burst firing in DA neurons thereby playing a key role in DA-dependent function and dysfunction[1,32]. Because astrocytes, as we show here, also induce a potentiation of these glutamatergic synapses, we next investigated whether *in vivo* astrocyte activation increases the burst firing mode of VTA DA neurons and eventually affects behavior. We injected AAV9-GFAP-hM3D(Gq)-mcherry or AAV5.GfaABC1D.cyto-tdTomato.SV40 in the VTA of adult male mice (Fig. 5a), specifically targeting astrocytes via the GFAP promoter (Extended Data Fig. 9). Astrocytes were activated through brief pressure pulses applied to a CNO-containing glass pipette, while recording the firing activity from individual VTA neurons that exhibit the typical features of DA neurons (Fig. 5a, b). Consistent with the astrocyte-mediated enhancement of glutamatergic transmission to DA neurons observed in VTA slices, VTA astrocyte activation by CNO increased the bursting discharges of all putative DA neurons that persisted for at least 10 min (Fig. 5c, e-f) and it also increased the overall firing rate in 5 out of 7 DA neurons (Fig. 5g, h). In contrast, the firing mode of DA neurons in tdTomato-expressing mice was unaffected by CNO, in terms of percentage of spikes in bursts and

281 firing rate (Fig. 5d-h). These *in vivo* data show that VTA astrocytes exert a direct control on
282 DA neuron firing activity.

283 We then asked whether the selective activation of VTA astrocytes, that increases the
284 burst firing of VTA DA neurons, could influence DA-dependent physiological functions. We
285 focused on motor activity, which is known to be controlled by DA. Notably, recent studies
286 revealed that DA neurons of the VTA, and not those of the Substantia Nigra (SN), play a
287 major role in the induction of motor hyperactivity[3,33,34]. Locomotion in an open field arena
288 was tested in male mice given bilateral VTA injections of AAV9-GFAP-hM3D(Gq)-mCherry
289 (hM3D) or AAV8-GFAP-GFP (GFP) (Fig. 6a, b). Thirty min after intraperitoneal injections,
290 CNO induced a locomotor hyperactivity in hM3D-injected mice as compared to GFP control
291 mice (Fig. 6c-e). The time spent at the center was similar in the two groups (Fig. 6f),
292 suggesting no major effects on anxiety-like phenotypes. Interestingly, the sustained
293 locomotor hyperactivity was still observed in hM3D mice 48 hrs after the CNO treatment
294 (Fig. 6c-e). Overall, these *in vivo* data show that activation of astrocytes in the VTA
295 enhances DA neuron firing activity and induces long-lasting motor hyperactivity.
296
297
298 **DISCUSSION**
299 The present study shows that astrocytes of the VTA, a key area in DA-dependent functions,
300 respond with Ca^{2+} elevations to eCBs and DA released by DA neurons and, in turn, induce
301 a long-lasting potentiation of glutamatergic synapses onto adjacent DA neurons. The
302 induction of this novel form of astrocyte-mediated plasticity is independent on NMDAR
303 activation and requires astrocytic Ca^{2+} elevations, presynaptic mGluR1 activation and NO
304 signalling. We also show that astrocyte activation *in vivo* increases the burst and the overall
305 firing rate of DA neurons and induces locomotor hyperactivity. These results indicate that

306 astrocytes play a key role in the modulation of VTA DA neuron circuits that control DA-
307 dependent physiological functions.

308 Astrocytes have been shown to respond with Ca^{2+} elevations to synaptic
309 neurotransmitters and release gliotransmitters that contribute to sensory information
310 processing and behavioral responses[13–15,35–38]. In different brain regions, including
311 hippocampus, dorsal striatum and neocortex, eCBs released by neurons at the somato-
312 dendritic level also recruit astrocytes evoking CB1R-mediated Ca^{2+} elevations and
313 gliotransmitter release that modulates synaptic transmission[18–20,39]. The present results
314 show that in the VTA, activation of both CB1 and D2Rs is required for astrocytic Ca^{2+}
315 elevations in response to DA neuron bursts and that these Ca^{2+} elevations in astrocytes are
316 crucial for bLTP generation. This is based on the following observations: 1) CB1 and D2Rs
317 are expressed and closely localized, in the same astrocyte; 2) astrocyte Ca^{2+} response to
318 DA neuron bursts and bLTP induction are abolished in the presence of specific antagonists
319 that block either the CB1 or the D2R; 3) DA neuron bursts fail to evoke bLTP following
320 deletion in VTA astrocytes of either the CB1 or the D2R; 4) bLTP could not be evoked after
321 the impairment of astrocytic Ca^{2+} elevations downstream the activation of CB1 and D2Rs;
322 5) bLTP can be rescued in young male mice upon selective chemogenetic activation of
323 astrocytes coupled to DA burst firing, even in the presence of the CB1 and D2R antagonists.
324 Notably, the results reported above in points 3-5, provide evidence that activation of
325 neuronal CB1 and D2Rs is not required for bLTP induction.

326 It is worth to further comment on results reported in point 3. In our experiments on
327 mice carrying the ‘‘floxed’’ CB1 or D2 gene and injected in the VTA with AAV9/2-hGFAP-
328 mCherry_iCre, we observed that the great majority of Cre-positive cells were astrocytes and
329 only about 5% were neurons (Extended Data Fig. 7). However, this approach may lead to
330 undetectable expression levels of the Cre recombinase and result in CB1 or D2R deletion
331 in a higher percentage of neurons[40]. It is noteworthy, however, that neuronal CB1 and D2Rs

in the VTA are inhibitory. Indeed, activation of presynaptic CB1 or D2Rs inhibits excitatory transmission onto VTA DA neurons[9,16] and activation of postsynaptic D2Rs induces a hyperpolarization that reduces VTA DA neuron excitability[9]. Furthermore, D2R activation in the VTA favors eCB-induced suppression of excitation[16]. These well-established inhibitory actions of neuronal CB1 and D2Rs in VTA circuitry are not consistent with the CB1 and D2R-dependent bLTP that we describe here and further support that activation of astrocytic rather than neuronal CB1 and D2Rs is required for bLTP generation.

Recent studies reported that astrocytes in different brain regions, including the VTA, express D1 and D2-type receptors and respond to bath applied DA stimuli with complex Ca^{2+} dynamics including regulation of basal cytosolic Ca^{2+} and repetitive Ca^{2+} transients[41–44]. Most interestingly, astrocytes in the NAc respond to synaptically released DA with D1R- rather than D2R-mediated Ca^{2+} elevations[44]. These data confirm that astrocytes of different brain regions and synaptic circuitries express different receptors that match the specific signals generated by distinct neuronal activities[13]. Consistent with this view, through the low affinity D1R, NAc astrocytes can sense the transient, high DA concentrations generated by synaptic release of DA from VTA DA projections[32]. Conversely, through the high affinity D2R[32], VTA astrocytes can sense the lower DA concentrations mainly generated in the VTA by somatodendritic rather than synaptic release and thus be functional targets of DA volume transmission[45].

An additional specificity of VTA astrocytes is that a cooperativity between CB1 and D2Rs is necessary for the Ca^{2+} response to DA neuron bursts, being activation of either CB1 or D2Rs alone insufficient to induce astrocytic Ca^{2+} elevations. Our EM immunogold experiments provide an ultrastructural background for this cooperativity revealing that CB1 and D2Rs are expressed in the same astrocytes, closely localized at astrocytic processes. Quantitative analysis from CB1/D2R double-labelled astrocytic processes also reveals that a group of couples exhibits an edge-to-edge separation $\leq$ 50 nm, which suggests physical

358 interactions between these two receptors and possible formation of heterodimers. Notably,
359 previous studies reported that D2 and CB1R coactivation in neurons enhances the formation
360 of CB1/D2R heterodimers[17,46]. Furthermore, we recently showed that coactivation of GABAb
361 and Somatostatin receptors in neocortical astrocytes confers signalling specificity between
362 different interneuron subtypes and astrocytes[47]. A cooperativity between different G-protein
363 coupled receptors may, therefore, be a general functional feature in the astrocyte response
364 to neuronal signals. Overall, CB1/D2R-expressing astrocytes in the VTA are fine-tuned to
365 sense eCB and dopamine releasing bursting neurons and extent excitation to neighboring
366 DA neurons through lateral potentiation of glutamatergic transmission. These results provide
367 further evidence for circuit- and synapse-specificity of neuron-astrocyte reciprocal signalling
368 in the brain[13].

369 The astrocyte-mediated bLTP is absent in young male mice in which DA neuron
370 bursts fail to elevate Ca^{2+} in astrocytes. Our data suggest that this failure is mainly due to a
371 lower expression of astrocytic CB1Rs in young with respect to adult male mice showing
372 regular bLTP. Importantly, bLTP could be rescued in young male mice by coupling DA
373 neuron bursts with Ca^{2+} elevations evoked by CNO in hM3D-expressing astrocytes. These
374 results further support a crucial role of astrocytic Ca^{2+} signals in bLTP induction mechanism.
375 It is noteworthy that the expression of mGlu1R in excitatory terminals is also significantly
376 lower in young with respect to adult male mice, suggesting that a defective neuronal
377 response to astrocytic glutamate may also contribute to the absence of bLTP in young male
378 mice.

379 In hippocampus, transient enhancement of excitatory transmission induced by
380 astrocytic glutamate becomes a long-lasting event when coupled with neuronal NO
381 release[19]. A similar mechanism appears operative in the VTA where in the absence of NO
382 only a transient (6 min) enhancement of glutamatergic transmission was observed.

383 Therefore, NO released by burst firing DA neurons is required for the sustained phase of
384 bLTP.

385 Astrocytic Ca^{2+} signalling is required for bLTP generation in both young female and
386 adult mice. However, while the mechanism downstream the astrocyte Ca^{2+} signaling
387 remains similar, IP_3R2 deletion in adult mice is insufficient to abolish bLTP. This finding
388 reveals an increased complexity in the regulatory mechanisms of astrocytic Ca^{2+} dynamics
389 during development with contribution of signalling pathways other than the IP_3R2-mediated
390 pathway[27,48]. From these observations it also follows that negative results on the role of
391 astrocytic Ca^{2+} signaling in $IP_3R2^{-/-}$ adult mice must be interpreted with caution.

392 Transient and/or persistent potentiation of glutamatergic synapses, fundamentally
393 mediated by NMDAR activation, regulate the burst firing mode of VTA DA neurons that plays
394 a pivotal role in DA-dependent behaviors[1,32]. The novel form of astrocyte-mediated
395 potentiation described here may integrate with these other forms of NMDAR-dependent
396 plasticity that favor the burst firing of DA neurons. Consistent with this view, we report that
397 *in vivo* astrocyte activation enhances DA neurons bursts and leads to a long-lasting
398 locomotor hyperactivity that recent studies revealed to depend on VTA rather than SN DA
399 neuron activity[3,33,34]. Present results also suggest that activation of astrocytes by burst firing
400 DA neurons and the consequent lateral potentiation of glutamatergic synapses, may
401 represent a strategy used by individual DA neurons to expand the burst firing mode to
402 neighboring DA neurons. Hence, it is possible that, through the fundamental recruitment of
403 astrocytes, an isolated, high bursting DA neuron favors the formation of spatially defined
404 clusters of coactive DA neurons that have been proposed to convey essential information
405 about a specific subset of behavioral variables to target regions[49]. Further specifically
406 designed experiments are necessary to validate this hypothesis.

407 Present results show that in the VTA circuitry, astrocyte signaling induces a long-
408 lasting potentiation of glutamatergic synapses to DA neurons, increases the burst firing

mode of DA neurons and favors locomotor hyperactivity thereby revealing an astrocyte-mediated mechanism in the control of DA neuron activity and DA-dependent behaviors. Our study also paves the way to future investigations examining whether dysregulations of DA neuron-astrocyte reciprocal communication within the VTA may contribute to the development of psychiatry disease states including motivation disorders, psychiatric disorders with a strong motor component, such as attention-deficit/hyperactivity disorder, and drug addiction.

METHODS

Animals and brain slice preparation. Animal care, handling and procedures were carried out in accordance with National (D.L. n.26, March 14, 2014) and European Community Council (2010/63/UE) laws, policies, and guidelines, and were approved by the local veterinary service. Horizontal VTA slices (240 µm) were obtained from both male and female C57BL/6J wild type (wt) mice and inositol 1,4,5-triphosphate-type 2 receptor (IP_3R2) knockout mice ($IP_3R2^{-/-}$)[50], and from male CB1R-[51] and D2R-flox[52] mice, at P14-17 (young mice) or P30-70 (adolescent/adult mice, to simplify adult mice). Animals were anesthetized with isofluorane, the brain removed and transferred into an ice-cold artificial cerebrospinal fluid (ACSF) containing (in mM): 125 NaCl, 2 KCl, 2 $CaCl_2$, 1 $MgCl_2$, 25 glucose, 25 $NaHCO_3$, 1.25 NaH_2PO_4, pH 7.4 with 95% O_2-5% CO_2. Slices were cut with a vibratome (Leica Vibratome VT1000S Mannhein, Germany) in the ice-cold solution described in Dugue at al. 2005[53] containing (in mM): 130 KGluconate, 15 KCl, 0.2 EGTA, 20 HEPES, 25 glucose, 2 Kynurenic acid. Slices were then transferred for 1 minute in a room-temperature solution containing (in mM): 225 D-mannitol, 2.5 KCl, 1.25 NaH_2PO_4, 26 $NaHCO_3$, 25 glucose, 0.8 $CaCl_2$, 8 $MgCl_2$, with 95% O_2-5% CO_2. Finally, slices were transferred in ACSF at 32°C for 15-20 minutes and then maintained at room temperature for the entire experiment.

Electrophysiological recordings and extracellular stimulation. Brain slices were continuously perfused in a submerged chamber with recording solution containing (in mM): NaCl 120; KCl 2; NaH_2PO4 1; $NaHCO_3$ 26; $MgCl_2$ 1; $CaCl_2$ 2; glucose 10; pH 7.4 (with 95% O_2-5% CO_2). Picrotoxin (50 µM) was added to block $GABA_A$ receptor currents. When indicated, other antagonists were bath applied with the recording solution. Cells were visualized with an Olympus FV1000 microscope (Olympus Optical, Tokyo, Japan). Conventional VTA DA neurons were recorded in the lateral part of the region medial to the

445 medial terminal nucleus of the accessory optical tract (mt, Fig. 1)[5,54]. DA neurons from the
446 lateral VTA were identified on the basis of their distinct morphology characterized by a large
447 and elongated soma with no particular dendritic orientation and the presence of the following
448 electrophysiological properties: a low-frequency tonic firing, a large I_h current elicited by
449 hyperpolarizing steps[16] and a slow depolarizing potential during current step injections[55]
450 (Extended Data Fig. 1 b-d). Simultaneous electrophysiological whole-cell patch-clamp
451 recordings from two DA neurons (distance of the somata, 70-120 µm) were made. Patch
452 electrodes (resistance, 3-4 MΩ) were filled with an internal solution containing (in mM): K-
453 gluconate, 135; KCl, 70; Hepes, 10; $MgCl_2$, 1; Na_2ATP 2 (pH 7.4 adjusted with KOH, 280-
454 290 mOsm/L). Recordings were obtained using a multiclamp-700B amplifier (Molecular
455 Device, Foster City, CA, USA). Signals were filtered at 1 kHz and acquired at 10 KHz
456 sampling rate with a DigiData 1440A interface board and pClamp 10 software. Series and
457 input resistances were monitored throughout the experiment using a 5 mV pulse.
458 Recordings were considered stable when the change of series and input resistances were
459 below 20%. Cells that do not meet these criteria were discharged. Theta capillaries filled
460 with recording solution were used for bipolar stimulation. To stimulate glutamatergic
461 afferents, electrodes were connected to an S-900 stimulator through an isolation unit and
462 placed 100-200 µm rostral to the recording electrode (Extended Data Fig. 1a). Paired pulses
463 (50 ms intervals) were delivered at 0.33 Hz. Excitatory post-synaptic currents (EPSCs) were
464 recorded while holding the membrane potential at -70 mV. Stimulus intensity was adjusted
465 to evoke 30-50 % maximal EPSCs. The EPSC amplitude was measured as the peak current
466 amplitude (2-9 ms after stimulus) minus the mean baseline current (100 ms before stimulus).
467 To illustrate the mean EPSCs time course, values were grouped in 3-min bins (i. e. mean
468 EPSCs from 60 stimuli). Changes in mean EPSCs in the first DA neuron were monitored
469 after imposing a burst or a tonic firing pattern to the second DA neuron (70-120 mm apart).
470 Burst firing pattern was imposed in current-clamp mode, through injections of intracellular

current pulses, with 5-pulse 20 Hz burst, every 500 ms for 5 min (Extended Data Fig. 1e)[23]. Tonic firing was imposed with individual current pulses applied at 2 Hz for 5 minutes[23] (Extended Data Fig. 1e). During the burst/tonic firing the extracellular stimulation was switched off. In electrophysiological experiments, time 0 indicates the end of the burst/tonic firing. For statistical analysis of short-term effects, mean EPSCs from 120 stimuli applied before (basal) and mean EPSCs from 60 stimuli applied during the first 3 min after the firing protocol (burst or tonic firing pattern) were compared. For statistical analysis of long-term effects, mean EPSCs from 120 stimuli applied before (basal), 24-30 min (indicated as 30 min time point in the bar chart) or 39-45 min (indicated as 45 min time point in the bar chart) after the firing protocol were compared. In young adult mice only the long-term effect at the time point of 30 min was analyzed due to the difficulty of obtaining long-lasting recordings in tissues from these mice. Paired-pulse ratio (PPR) was calculated as 2nd EPSC/1st EPSC and evaluation of the PPR before and after the burst firing protocol was used to identify the pre- or postsynaptic locus of the bLTP.

Dye loading and Ca^{2+} imaging experiments. Slices were loaded with the astrocyte specific marker Sulforhodamine 101 (SR101) (0.3 µM, Sigma Aldrich, Milano) in ACSF at 32°C for 15 minutes. Then, slices were loaded for 45 min at room temperature with the Ca^{2+} sensitive dye Fluo4-AM (7,6 µM, Life Technologies, Monza, IT) in an ACSF solution containing pluronic F-127 (0.0067%, Sigma Aldrich, Milano, IT) and bubbled with 95% O_2-5% CO_2. Ca^{2+} imaging experiments were conducted with a confocal laser scanning microscope TCS-SP5-RS (Leica Microsystems, GmbH, Wetzlar, Germany) equipped with two solid state lasers tuned at 448 nm and 543 nm (to image Fluo-4 and SR101 fluorescence, respectively) and a 20x objective (NA, 1.0). Images were acquired with a 0.5 Hz frame rate for 90s, with time intervals of 5 min between recordings. Image sequences were processed with ImageJ. Regions of interest (ROIs) were drawn around cellular somata using the red SR101 signal.

497 Ca^{2+} events were estimated as changes of the Fluo-4 fluorescence signal over baseline
498 ($\Delta F/F_0 = (F(t)-F_0)/F_0$). A fluorescence increase was considered a significant event when it
499 exceeded two times the standard deviation from the baseline. Astrocyte Ca^{2+} responses
500 were quantified by analyzing the probability of occurrence of Ca^{2+} spike by detecting the
501 onset of Ca^{2+} elevations (Ca^{2+} spikes) during the recording period. To investigate the
502 astrocyte response to the burst firing of DA neurons, a DA neuron was patch with an
503 intracellular solution (see details before) containing the fluorescent tracer Neurobiotin 488
504 (65 μM, Vector Laboratories, Inc, USA) to visualize neuronal soma and dendrites. To obtain
505 the time course of the Ca^{2+} spike probability index reported in figures 1 and 2, the number
506 of astrocytic Ca^{2+} spikes for each recording period was divided by the number of SR101-
507 positive astrocytes in proximity (around 50 μm) to Neurobiotin 488-filled DA neuron soma
508 and dendrites. After three basal recordings, a burst firing pattern was imposed to the DA
509 neuron (in current-clamp mode, through injections of intracellular current pulses, with 5-
510 pulse 20 Hz burst, every 500 ms for 5 min) and the quantification of the Ca^{2+} spike probability
511 was resumed 4.5 min after the initiation of the burst firing. In Ca^{2+} imaging experiments, time
512 0 indicates the start of the burst firing. For statistical analysis, a mean value of the Ca^{2+} spike
513 probability/min per slice was calculated at basal conditions (mean of the three basal
514 recordings) and after DA neuronal burst firing (mean of 4 consecutive recordings after the
515 burst firing, the first at a time point of 4.5 min after the burst firing and the last at a time point
516 of 24 min after the burst firing). When indicated, Ca^{2+} imaging experiments were performed
517 in slices expressing the genetically encoded Ca^{2+} indicator GCaMP6f and the Gq protein-
518 coupled designer receptor exclusively activated by designer drugs (DREADDs) hM3D in
519 astrocytes (for AAVs delivery details see below). In these experiments, Ca^{2+} elevations were
520 evoked by bath perfusion of the hM3D agonist clozapine N-oxide CNO (10 μM) 2.5 min after
521 the start of the burst firing. A mean time course of the Ca^{2+} response to CNO was calculated

522 by plotting the $\Delta F/F_0$ of a ROI drawn around the entire recording field. Then, plots were
523 aligned for the Ca^{2+} peak to calculate the mean time course of the Ca^{2+} response to CNO.
524
525 **AAVs delivery.** We bilaterally injected in the VTA of C57BL6J wild-type male mice, at
526 postnatal days 0-2 or 28-30, the viral vector ssAAV-9/2-hGFAP-hM3D(Gq)_mCherry-
527 WPRE-hGHp(A) (VVF-UZH, Zurich, Switzerland, 4.6 x 10E12 viral genomes (vg)/ml), that
528 contains the astrocytic promoter to selectively express in astrocytes the mCherry-tagged,
529 Gq-coupled Designer Receptors Activated Only by Designer Drugs (DREADD) hM3D. Two-
530 three weeks after injection, we performed electrophysiological experiments in brain slices
531 from juvenile mice (P14-17) and in vivo single unit recordings in adult mice (P45-50). As
532 control for single unit recording experiments, in the VTA of wild-type male mice we bilaterally
533 injected the viral vector AAV5.GfaABC1D.cyto-tdTomato.SV40 (Addgene, USA, 2.4x 10E13
534 vg/ml), that carries the astrocytic promoter GfaABC1D to express selectively in astrocytes
535 the tdTomato marker. In a group of P0-P2 mice, both ssAAV-9/2-hGFAP-
536 hM3D(Gq)_mCherry-WPRE-hGHp(A) and AAV5.GfaABC1D.cytoGCaMP6f.SV40
537 (Addgene, USA, 1.81 x 10E13 genome copies/ml) viral vectors were injected together to
538 assess the Ca^{2+} responses evoked in astrocytes after activation of hM3D, using the Ca^{2+}
539 indicator GCaMP6f. To selectively express the Cre recombinase in astrocytes, injections of
540 the viral vector ssAAV9/2-hGFAP-mCherry_iCre-WPRE-hGHp(A) (VVF-UZH, Zurich,
541 Switzerland, 5.2 x 10E12 vector genomes/ml) carrying the astrocytic promoter GfaABC1D
542 were bilaterally performed in the VTA of P 28-30 male mice containing the D2R or the CB1R
543 floxed gene. As control mice, the same viral vector was injected in age-matched C57BL6J
544 wild-type mice. Brain slice electrophysiological experiments were performed 4 weeks after
545 injection. AAV5.GfaABC1D.mCherry.hPMCA2w/b.SV40 (Penn Vector Core, USA, 1.14 x
546 10E13 genome copies/ml) was bilaterally injected in the VTA of both female and male $IP_3R2^{-/-}$
547 mice, at postnatal days 28-30, to selectively express in astrocytes the Ca^{2+} pump

hPMCA2w/b[31]. Brain slice electrophysiological experiments were performed 4 weeks after injection. AAV5.GfaABC1D.mCherry.hPMCA2w/b.SV40 was injected without previous dilution. The other viral vectors were diluted to 50% in ACSF before injection. When two viral vectors were injected, both vectors were present at a 1:1 ratio. The coordinates for viral injections were (in mm): AP 0.1, ML ± 0.15, DV -3.8 from lambda for P0-2 mice; AP -3.0, ML ± 0.5, DV -4.4 from Bregma for P28-30 mice. For injections in P0 mice, animals were anesthetized by hypothermia for three minutes and fixed into a modeled platform. Using a manually graduated pull glassed pipette, connected to a costume-made pressure injection system, we punch the skull bilaterally and injected a total volume of 350 nl containing the viral vector. After injection, the skin was sutured and mice were revitalized under a heat lamp before returning to their cage. For injections in P28-30 mice, animals were anesthetized with isoflurane (induction 4-5%, maintenance 1-2%). Depth of anesthesia was assured by monitoring respiration rate, eyelid reflex, vibrissae movements, and reactions to pinching the tail and toe. After drilling two holes into the skull over the VTA, we injected a total volume of 500 nl by using a pulled glass pipette connected to a peristaltic pump, at a rate of 100 nl/min. Pipette was kept for 10 minutes in the tissue before slow withdrawal. After injections, the skin was sutured and mice were revitalized under a heat lamp and returned to their cage.

Immuhistochemistry and cell counting. For the evaluation of the number of mCherry expressing astrocytes and neurons we prepared 70 µm thick brain slices from young and adult animals injected with ssAAV-9/2-hGFAP-hM3D(Gq)_mCherry-WPRE-hGHp(A), ssAAV9/2-hGFAP-mCherry_iCre-WPRE-hGHp(A) or AAV5.GfaABC1D.mCherry.hPMCA2w/b.SV40. Mice were euthanized with 5% isoflurane and transcardially perfused with PBS followed by ice-cold 4% PFA in PBS. Brains were removed and postfixed overnight at 4°C in the same fixative solution. Horizontal brain slices were obtained with a VT1000S

vibratome (Leica), collected as floating sections and blocked for 1 hr in the Blocking Serum (BS: 1% BSA, 2% goat serum and 1% horse serum in PBS) and 0,2% TritonX-100. After blocking, sections were incubated (overnight at 4°C) with the following primary antibodies in BS plus 0,02% Tx-100: anti-NeuN (RRID:AB_2298772, 1:200 mouse, Thermofisher_Millipore MAB377), anti-glial fibrillary acidic protein (GFAP, RRID:AB_10013382, 1:400 rabbit, Dako Agilent , Z0334), anti-S100B (RRID:AB_2315306, 1:400 rabbit, Dako Agilent, Z031129), anti-glutamate transporter 1 (GLT1, RRID:AB_90949, 1:400 guinea pig, Abcam, AB1783); prefixed in 50% methanol in PBS per 15 minutes). After washing with PBS, slices were incubated for 2 hr at room temperature with secondary antibodies conjugated with AlexaFluor-488 (1:500; A21202 donkey anti-mouse; A21206 donkey anti-rabbit; A11073 goat anti-guinea pig, Invitrogen Thermo-Scientific). To evaluate mCherry positive cells, we directly evaluate the red fluorescence of infected slices. Only for $IP_3R2^{-/-}$ mice injected with AAV5.GfaABC1D.mCherry.hPMCA2w/b.SV40, we performed double immunofluorescence of NeuN (or GLT1) together with anti-RFP (RRID:AB_2209751, 1:1000 rabbit, Rockland , 600-401-379). In this case, secondary antibodies were anti-mouse (or anti-guinea pig) AlexaFluor-488 conjugated together the anti-rabbit AlexaFluor-555 conjugated (A21430 donkey anti-rabbit, Invitrogen Thermo-Scientific, 1:500). Slices were then washed and nuclei were stained with Top-Ro3 (Invitrogen Thermo-Scientific, 1:1000). Negative controls were performed in the absence of the primary antibodies. We used a TCS-SP5-RS laser scanning microscope (Leica, Germany; 20x NA1x/W objective) to acquire sequential three channels, confocal image z-stacks (1 µm z-step, 456,33x456,33 µm) and ImageJ for double-labeled cell counting. We counted mCherry-positive cells and then we evaluated the percentage of mCherry-positive cells that were neurons (mCherry+/NeuN+) or glial cells. VTA from both hemispheres of injected animals was evaluated in at least two mice for each group.

Pre- and post-embedding electron microscopy. Animals. Seven P16 and four P50 C57BL/6 mice (3 females, 4 males for P16; 2 females and 2 males for P50) were used. Mice were anesthetized with an intraperitoneal injection of chloral hydrate (300 mg/kg) and perfused transcardially with a flush of saline solution followed by 4% freshly depolymerized paraformaldehyde and 0.2% glutaraldehyde in 0.1 M phosphate buffer (PB; pH 7.4). Brains were removed, post-fixed in the same fixative (for 48 hrs), and cut on a Vibratome in 50 µm serial horizontal sections from the midbrain which were collected in PB until processing[56]. Horizontal sections were through the dorso-ventral extent of ventral tegmental area (VTA) resulting in 7-8 sections per series. In order to verify the dorso-ventral extension of VTA, a pilot series of sections from a male mouse, were immuno-processed for tyrosine-hydroxylase (primary antibodies from Millipore, AB1542, RRID:AB_90755[57]; 1:500) and for Nissl staining. In immunoreacted sections (see data collection and analysis) lateral VTA was identified as the region medial to the medial terminal nucleus of the accessory optical tract[5,54] (MT). Information on antibodies used for electron microscopy are reported in Table 1.

Immunoperoxidase and pre-embedding procedures. Sections were treated with H_2O_2 (1% in PB; 30 min) to remove endogenous peroxidase activity, rinsed in PB and pre-incubated in 10% normal goat serum (NGS, 1 hr; for mGLUR1α, mGlur1β, D2, D3, D4) or in 10 % normal donkey serum (NDS, 1 hr; for CB1). Sections were then incubated in a solution containing primary antibodies (see Table 1 for dilutions; 2 hrs at room temperature [RT] and overnight at 4°C). The following day, sections were rinsed 3 times in PB and incubated first in 10% NGS or 10% NDS (15 min) and then in a solution containing secondary biotinylated secondary antibodies (see Table 1 for dilutions; 1.5 hr at RT). Sections were subsequently rinsed in PB, incubated in avidin-biotin peroxidase complex (ABC Elite PK6100, Vector), washed several times in PB, and incubated in 3,3'diaminobenzidine tetrahydrochloride (DAB; 0.05% in 0.05 M Tris buffer, pH 7.6 with 0.03% H2O2). Method specificity was verified by substituting primary antibodies with PB or

626 NGS. As previously described[56] after completion of immunoperoxidase procedures,
627 sections were post-fixed in 1% osmium tetroxide in PB for 45 m and contrasted with 1%
628 uranyl acetate in maleate buffer (pH 6.0; 1 h). After dehydration in ethanol and propylene
629 oxide, sections were embedded in Epon/Spurr resin (Electron Microscopy Sciences,
630 Hatfield, PA, USA), flattened between Aclar sheets (Electron Microscopy Sciences) and
631 polymerized at 60°C for (48 hrs). Chips including lateral VTA were selected by light-
632 microscopic inspection, glued to blank epoxy and sectioned with an ultramicrotome (MTX;
633 Research and Manufactoring Company Inc., Tucson, AZ, USA). The most superficial
634 ultrathin sections (~60 nm) were collected and mounted on 300 mesh nickel grids, stained
635 with Sato's lead and examined with a Philips EM 208 and CM10 electron microscopes
636 coupled to a MegaView-II high resolution CCD camera (Soft Imaging System). To minimize
637 the effects of procedural variables, all material from P16 and P50 females and males was
638 processed in parallel.

639 Post-embedding procedures. Sections were processed for an osmium-free
640 embedding method[58]. Dehydrated sections were immersed in propylene oxide, infiltrated
641 with a mixture of Epon/Spurr resins, sandwiched between Aclar films, and polymerized at
642 60 °C for 48 h. After polymerization, chips were cut from the wafers, glued to blank resin
643 blocks and sectioned with an ultramicrotome. Thin sections (60–80 nm) were cut and
644 mounted on 300 mesh nickel grids and processed for immunogold labeling[58,59]. In brief, after
645 treatment with 4 % para-phenylenediamine in Tris-buffered saline [0.1 M Tris, pH 7.6, with
646 0.005 %Tergitol NP-10 (TBST)], grids were washed in TBST (pH 7.6), transferred for 15 min
647 in 0.25% NDS in TBST (pH 7.6) and then incubated overnight (26°C) in a solution of TBST
648 (pH 7.6) containing a mixture of anti-D2 and anti-CB1 primary antibodies (see Table 1 for
649 dilutions). Grids were subsequently washed in TBST (pH 8.2), transferred for 10 min in 0.5%
650 NDS in TBST (pH 8.2), incubated for 2 hrs (26°C) in TBST (pH 8.2) containing secondary
651 antibodies conjugated to 18 and 12 nm gold particles, washed in distilled water, and then

652 stained with uranyl acetate and Sato's lead. The optimal concentration of antibodies to D2
653 and CB1Rs was sought by testing several dilutions; the concentration yielding the lowest
654 level of background labeling and still immunopositive elements was used to perform the final
655 studies. Gold particles were not detected when primary antiserum was omitted. When
656 normal serum was substituted for immune serum, sparse and scattered gold particles were
657 observed, but they did not show any specific relationship to subcellular compartments.
658 Data collection and analysis. All data were obtained from lateral VTA of
659 immunoreacted sections[5,54].
660 For pre-embedding electron microscopy, mGluR1α, mGluR1β, CB1, D2, D3, D4R
661 immunoreactive profiles were studied in ultrathin sections from the surface of the embedded
662 blocks. Quantitative data derived from the analysis of microscopic fields of lateral VTA (10–
663 12 ultrathin sections/animal) selected and captured at original magnifications of 12,000x-
664 30,000x. Microscopical fields from females and males containing positive processes were
665 randomly selected. Acquisition of microscopical fields and analysis of female and male mice
666 were performed under blinded conditions.
667 For the analysis of the distribution of mGluR1α, mGluR1β, CB1, D2, D3, D4R positive
668 profiles, subcellular compartments were identified according to well-established criteria[60]
669 (Extended Data Figures and Tables 1 and 2). For quantifying mGluR1α or mGluR1β in P16
670 VTA, and mGluR1β in P50 VTA at axon terminals, synapses exclusively characterized by a
671 presynaptic terminal with clear and round vesicles nearby the presynaptic density, a synaptic
672 cleft displaying electron dense material, pre- and postsynaptic membranes defining the
673 active zone and the post-synaptic specialization, and finally by a prominent postsynaptic
674 density the asymmetric synapses[60,61] were sampled (axon terminals making asymmetric
675 synaptic contacts containing one or more dense core vesicles more likely representative of
676 co-release of glutamate and others neurotransmitters[62–64] were not included in this group;
677 Tables 2 and 4).

For quantifying CB1, D2, D3, D4R at astrocytic processes in P16 VTA, and CB1 and D2R in P50 VTA, astrocytic profiles were identified based on their typical irregular outlines and the paucity of cytoplasmic components (with the exception of ribosomes, glycogen granules and various fibrils[60]. For post-embedding electron microscopy, ultrathin sections (20 ultrathin sections/animal) were examined at 50,000–85,000x and fields that included at least 1 double immunolabeled astrocytic profile were selected. For determining the relative density of D2 and CB1Rs at the membranes of double labeled astrocytic profiles, pyramidal cell nuclei were also identified: gold particles within labeled structures were counted and areas were calculated using ImageJ (NIH, Bethesda, MD, USA). Background was calculated by estimating labeling density over pyramidal cell nuclei[59,65]. Particle densities were counted and compared with background labeling. Gold particles were considered associated with plasma membrane if they were within 20 nm of the extracellular side of the membrane. To determine the degree of nearness of D2 and CB1R at the membrane of double-labeled profiles the edge-to-edge distances between immunogold labeled D2 and CB1R were measured along the membrane using ImageJ and the distribution of the separation distances between D2 and CB1R was determined[47,59,66–69]. In the cases in which multiple paths connecting particles gave different inter-distance values, the shortest inter-distance was selected and used for distribution analysis. Given that gold particles with edge-to-edge separation distance ≤50 nm are highly suggestive of physical interactions of two detected proteins (i.e., a physical coupling complex[47,59,66–69]) distribution analysis of the interdistance between particles was based on bin of 50 nm.

For all microscopy data, normality tests and statistical analyses were performed using GraphPad Prism Software v.7.0a (San Diego, CA, USA).

706 Table 1. Primary and Secondary antibodies

Protein	Source	Primary antibody	Host	Characterized in	Dilution	Secondary antibody	Source	Dilution
mGLUR1α	Frontier Institute	Rb-Af811 (RRID:AB_257179)	Rb	Ohtani et al. 2014[a]	1:200	Biotinylated	Jackson	1:500
mGLUR1β	Frontier Institute	Rb-Af250 (RRID: AB_2616586)	Rb	Ohtani et al. 2014[b]	1:100	Biotinylated	Jackson	1:500
CB1	Frontier Institute	GP-Af530 (RRID: AB_2571593)	GP	Garcia-Ovejero et al. 2013[c]	1:200 IP 1:25 IG	Biotinylated 18 nm gold	Jackson Jackson	1:500 1:20
D2	Millipore	AB5084P (RRID:AB_2094980)	Rb	Stojanovic et al. 2017[d]	1:100 IP 1:10 IG	Biotinylated 12 nm gold	Jackson Jackson	1:500 1:20
D3	Alomone	ADR-003 (RRID:AB_2039830)	Rb	Solís et al. 2017 Castro-Hernandez et al. 2015[e]	1:100	Biotinylated	Jackson	1:500
D4	Millipore	AB324405 (RRID:AB_564550)	Rb	Barili et al. 2000[f]	1:1000	Biotinylated	Jackson	1:500

707
708
709 Abbreviations: IP, immunoperoxidase for pre-embedding electron microscopy; IG,
710 immunogold for post-embedding electron microscopy.
711
712 [a] Raised against a synthetic peptide corresponding to AA 945-1127 of mouse mGLUR1α.
713 Immunoreactivity verified in mGluR1 knock-out mice[70].

714 [b] Raised against a synthetic peptide corresponding to AA 899-906 of mouse mGLUR1β.
715 Immunoreactivity verified in mGluR1 knock-out mice[70].

716 [c] Raised against the C-terminal 31 AA of mouse CB1. Lack of immunoreactivity in CB1
717 knock-out mice[71].

718 [d] Raised against a peptide corresponding to 28 AA within the third cytoplasmic loop of
719 human D2 receptor. Lack of immunoreactivity in D2 knock-out mice[72].

720 [e] Raised against a synthetic peptide corresponding to AA 15-29 within the extracellular N-
721 terminus sequence of rat D3 receptor. Lack of immunoreactivity in D3 knock-out mice[73,74].

722 [f] Raised against a synthetic peptide corresponding to AA 176-185 of human D4 receptor.
723 Immunoreactivity totally abolished by preadsorption of D4 antibodies with immunogen
724 peptide[75].

725

***In vivo* single unit recordings.** C57BL/6J wild-type male mice, injected 2-3 weeks before with ssAAV-9/2-hGFAP-hM3D(Gq)_mCherry-WPRE-hGHp(A) or AAV5.GfaABC1D.cyto-tdTomato.SV40, were anesthetized using chloral hydrate (400 mg/kg i.p.), supplemented as required to maintain optimal anesthesia throughout the experiment, and placed in the stereotaxic apparatus (Kopf, Germany). Their body temperature was maintained at 36 ± 1 °C using a feedback-controlled heating pad. For the placement of a recording electrode, the scalp was retracted and one burr hole was drilled above the parabrachial pigmented nuclei of the posterior VTA (AP: - 3.0-3.5 mm from bregma; L: 0.4-0.6 mm from midline; V: 4-5 mm from the cortical surface) according to the Paxinos and Franklin atlas (2004). Extracellular identification of putative DA neurons was based on their location as well as on the set of electrophysiological features that characterize these cells *in vivo*: (1) a typical triphasic action potential with a marked negative deflection; (2) an action potential width from start to end > 2.5 ms; (3) a slow firing rate (< 10 Hz). VTA putative DA neurons were selected only when all the already published criteria were fulfilled[76–79]. Single unit activity of putative DA neurons was recorded extracellularly using glass micropipettes filled with 2% Chicago sky blue dissolved in 0.5 M sodium acetate (impedance 3-7 MΩ). An injection pipette (20-40 µm in diameter attached ~150-100 µm above the recording tip) was used for simultaneous local microinjection of CNO (1 mM). Signal was pre-amplified, amplified (Neurolog System, Digitimer, UK), filtered (band-pass 500–5000 Hz), and displayed on a digital storage oscilloscope. Experiments were sampled on- and off-line by a computer connected to CED Power 1401 laboratory interface (Cambridge Electronic Design, Cambridge, UK) running the Spike2 software (Cambridge Electronic Design, Cambridge).

Single units were isolated and the spontaneous activity recorded for a minimum of 3 min before local application of CNO (1 mM). A total volume of 30-100 nl was infused using brief (10-100 ms) pressure pulses (40 psi, Picospritzer, Narishige, Japan). One injection maximum per hemisphere was given. For statistical analysis, we calculated the mean firing

752 rate (number of spikes/s) and the percentage of spikes in burst (SiB), before and after CNO
753 application (in 2-min bins or in the 10 min of recording after CNO application). Bursts were
754 defined as the occurrence of two spikes at an inter-spike interval of < 80 ms, and terminated
755 when the inter-spike interval exceeded 160 ms[80]. At the end of the experiment, negative
756 DC (15 mA for 5 minutes) was passed through the recording electrode to eject Pontamine
757 sky blue, which allowed the anatomical location of the recorded neuron. Mice were then
758 euthanized and brains were rapidly removed and fixed in 4% paraformaldehyde solution.
759 The position of the electrodes was identified with a microscope in coronal sections (100 µm).
760 Only recordings in the correct area were considered for analysis.
761
762 **Behavioral test.** Viral Injection. C57BL/6J mice were naïve and two month-old at the time
763 of surgery. All mice were anesthetized with a mix of isoflurane/oxygen 2%/1% by inhalation
764 and mounted into a stereotaxic frame (Kopf). Brain coordinates of viral injections in the VTA
765 were chosen in accordance with the mouse brain atlas: AP: -3 mm; ML: ± 0.50 mm; DV: -
766 4.7 mm. The volume of AAV injection (AAV9-GFAP-hM3D(Gq)-mcherry or AAV8-GFAP-
767 GFP) was 100 nl per hemisphere. We infused virus through a glass micropipette connected
768 to a 10-µL Hamilton syringe. After infusion, the pipette was kept in place for 6 min and then
769 slowly withdrawn.
770 Locomotor Activity. Mice were tested during first two hours of the dark phase in an
771 experimental apparatus consisting of 4 grey, opaque open field boxes (40x40x40 cm) evenly
772 illuminated by overhead lighting (5 ± 1 lux). Each session was video recorded with ANY-
773 maze tracking software (Stoelting Co.) for one hour. In the first day of locomotor activity all
774 animal received an injection of CNO (3mg/kg) 30 minutes before the beginning of the test;
775 48 hours later, the animals have been tested for a second time in the same apparatus with
776 a saline injection.
777

Drugs. Picrotoxin 50 µM (SIGMA, Aldrich, Milano, IT); AM251 2-4 µM (Abcam, Cambridge, UK); eticlopride hydrochloride 1 µM (Abcam, Cambridge, UK); SCH-23390 hydrochloride 10 µM (Abcam, Cambridge, UK); D-AP5 50 µM (Abcam, Cambridge, UK); LY-367385 100 µM (Abcam, Cambridge, UK); clozapine-N-oxide (CNO) 10 µM (MedChemExpress, USA) and L-741,626 10 µM (Tocris, Bristol, UK) were bath applied. L-NAME 100 µM (SIGMA, Aldrich, Milano, IT) was included in the patch pipette.

Data analysis. Data analysis was performed with Clampfit 10.5, Origin 8.0 (Microcal Software), Microsoft Excel 2010, ImageJ (NHI), Sigma Plot 11, ANY-maze tracking software and GraphPad Prism 7.0a.

Statistical analysis. No statistical methods were used to predetermine sample size. Data are expressed as mean ± standard error of the mean (SEM). Normality test (Shaphiro-Wilk test) was applied to the data before running statistical tests. Based on the normality test result, data were analyzed using either parametric (two-tailed Student's t-test) or nonparametric tests (Wilcoxon signed-rank test) as appropriate. For electron microscopy data analysis, Mann-Whitney test and contingency Fisher's test were used. For *in vivo* single unit recordings and behavioral tests, two-way RM ANOVA and Bonferroni's multiple comparison test was used. Statistical differences were established with $p < 0.05$ (*), $p < 0.01$ (**), $p < 0.001$ (***) and $p < 0.0001$ (****).

ACKNOWLEDGEMENTS

We are grateful to all the members of Dr. Carmignoto's laboratory and to M. Melis, M. Sessolo, G. Colombo and M. Santoni for helpful discussion and suggestions. We also thank T. Pozzan for his valuable comments on the manuscript and discussions, M. Morini, D. Cantatore, B. Chiarenza, A. Monteforte and C. Chiabrera for technical support and Dr. Chen

for kindly providing $IP_3R2^{-/-}$ mice. This research was supported by European Commission (H2020-MSCA-ITN, 722053 EU-GliaPhD), PRIN 2015-W2N883_001, Premiale CNR-TERABIO, 2017 Premiale MIUR - nano4BRAIN to GC, the Istituto Italiano di Tecnologia and the Ministero della Salute italiano (project GR-2016-02362413) to FP, grants from UNIVPM (PSA#040046) and by Fondazione di Medicina Molecolare to FC, European Brain Research Institute (EBRI)/National Research Council of Italy (CNR) collaborative agreement to ALM, GC.

AUTHOR CONTRIBUTIONS

LMR, MGG and GC designed the study. LMR and MGG performed the electrophysiological and Ca^{2+} imaging experiments in brain slices. AC performed the immunohistochemistry experiments. FM, GP and FP performed the behavioral experiments. MC and ALM performed the in vivo single unit recordings. MM, AP and FC performed the electron microscopy experiments. GM provided the CB1-floxed mice. All authors discussed the results. MGG and GC wrote the paper with inputs from all the authors.

COMPETING INTERESTS

The authors declare no competing interests.

REFERENCES

1. Pignatelli, M. & Bonci, A. Role of Dopamine Neurons in Reward and Aversion: A Synaptic Plasticity Perspective. *Neuron* **86**, 1145–1157 (2015).
2. Thiele, A. & Bellgrove, M. A. Neuromodulation of Attention. *Neuron* vol. 97 769–785 (2018).
3. Runegaard, A. H. *et al.* Modulating dopamine signaling and behavior with chemogenetics: Concepts, progress, and challenges. *Pharmacol. Rev.* **71**, 123–156

(2019).

4. Paladini, C. A. & Roeper, J. Generating bursts (and pauses) in the dopamine midbrain neurons. *Neuroscience* **282**, 109–121 (2014).

5. Morales, M. & Margolis, E. B. Ventral tegmental area: Cellular heterogeneity, connectivity and behaviour. *Nat. Rev. Neurosci.* **18**, 73–85 (2017).

6. Poulin, J. F. *et al.* Mapping projections of molecularly defined dopamine neuron subtypes using intersectional genetic approaches. *Nat. Neurosci.* **21**, 1260–1271 (2018).

7. Beier, K. T. *et al.* Circuit Architecture of VTA Dopamine Neurons Revealed by Systematic Input-Output Mapping. *Cell* **162**, 622–634 (2015).

8. Watabe-Uchida, M., Zhu, L., Ogawa, S. K., Vamanrao, A. & Uchida, N. Whole-Brain Mapping of Direct Inputs to Midbrain Dopamine Neurons. *Neuron* **74**, 858–873 (2012).

9. Morikawa, H. & Paladini, C. A. Dynamic regulation of midbrain dopamine neuron activity: Intrinsic, synaptic, and plasticity mechanisms. *Neuroscience* **198**, 95–111 (2011).

10. Bonci, A. & Malenka, R. C. Properties and plasticity of excitatory synapses on dopaminergic and GABAergic cells in the ventral tegmental area. *J. Neurosci.* **19**, 3723–3730 (1999).

11. Gomez, J. A. *et al.* Ventral tegmental area astrocytes orchestrate avoidance and approach behavior. *Nat. Commun.* **10**, 1–13 (2019).

12. Octeau, J. C. *et al.* Transient, Consequential Increases in Extracellular Potassium Ions Accompany Channelrhodopsin2 Excitation. *Cell Rep.* **27**, 2249-2261.e7 (2019).

13. Araque, A. *et al.* Gliotransmitters travel in time and space. *Neuron* **81**, 728–739 (2014).

14. Bazargani, N. & Attwell, D. Astrocyte calcium signaling: the third wave. *Nat. Neurosci.* **19**, 182–189 (2016).

856 15. Volterra, A., Liaudet, N. & Savtchouk, I. Astrocyte Ca2+ signalling: an unexpected
857 complexity. *Nat. Rev. Neurosci.* **15**, 327–335 (2014).
858 16. Melis, M. *et al.* Endocannabinoids Mediate Presynaptic Inhibition of Glutamatergic
859 Transmission in Rat Ventral Tegmental Area Dopamine Neurons through Activation
860 of CB1 Receptors. *J. Neurosci.* **24**, 53–62 (2004).
861 17. Busquets-Garcia, A., Bains, J. & Marsicano, G. CB1 Receptor Signaling in the Brain:
862 Extracting Specificity from Ubiquity. *Neuropsychopharmacology* **43**, 4–20 (2018).
863 18. Navarrete, M. & Araque, A. Endocannabinoids potentiate synaptic transmission
864 through stimulation of astrocytes. *Neuron* **68**, 113–126 (2010).
865 19. Gómez-Gonzalo, M. *et al.* Endocannabinoids induce lateral long-term potentiation of
866 transmitter release by stimulation of gliotransmission. *Cereb. Cortex* **25**, (2015).
867 20. Martín, R., Bajo-Grañeras, R., Moratalla, R., Perea, G. & Araque, A. Circuit-specific
868 signaling in astrocyte-neuron networks in basal ganglia pathways. *Science (80-.).*
869 **349**, 730–734 (2015).
870 21. Wang, H. & Lupica, C. R. Release of endogenous cannabinoids from ventral
871 tegmental area dopamine neurons and the modulation of synaptic processes. *Prog.*
872 *Neuro-Psychopharmacology Biol. Psychiatry* **52**, 24–27 (2014).
873 22. Rice, M. E. & Patel, J. C. Somatodendritic dopamine release: Recent mechanistic
874 insights. *Philos. Trans. R. Soc. B Biol. Sci.* **370**, 1–14 (2015).
875 23. Lalive, A. L. *et al.* Firing modes of dopamine neurons drive bidirectional GIRK channel
876 plasticity. *J. Neurosci.* **34**, 5107–5114 (2014).
877 24. Lohani, S. *et al.* Burst activation of dopamine neurons produces prolonged post-burst
878 availability of actively released dopamine. *Neuropsychopharmacology* **43**, 2083–2092
879 (2018).
880 25. Dahan, L. *et al.* Prominent burst firing of dopaminergic neurons in the ventral
881 tegmental area during paradoxical sleep. *Neuropsychopharmacology* **32**, 1232–1241

(2007).

26. Srinivasan, R. *et al.* Ca2+ signaling in astrocytes from Ip3r2 -/- mice in brain slices and during startle responses in vivo. *Nat. Neurosci.* **18**, 708–717 (2015).

27. Agarwal, A. *et al.* Transient Opening of the Mitochondrial Permeability Transition Pore Induces Microdomain Calcium Transients in Astrocyte Processes. *Neuron* **93**, (2017).

28. Lüscher, C. & Malenka, R. C. NMDA Receptor-Dependent Long-Term Potentation and Long-Term Depression (LTP/LTD). *Cold Spring Harb. Perspect. Biol.* **4**, a005710 (2012).

29. Hardingham, N., Dachtler, J. & Fox, K. The role of nitric oxide in pre-synaptic plasticity and homeostasis. *Front. Cell. Neurosci.* **7**, 1–19 (2013).

30. Pasti, L., Pozzan, T. & Carmignoto, G. Long-lasting changes of calcium oscillations in astrocytes. A new form of glutamate-mediated plasticity. *Journal of Biological Chemistry* vol. 270 15203–15210 (1995).

31. Yu, X. *et al.* Reducing Astrocyte Calcium Signaling In Vivo Alters Striatal Microcircuits and Causes Repetitive Behavior. *Neuron* **99**, 1170-1187.e9 (2018).

32. Grace, A. A., Floresco, S. B., Goto, Y. & Lodge, D. J. Regulation of firing of dopaminergic neurons and control of goal-directed behaviors. *Trends Neurosci.* **30**, 220–227 (2007).

33. Boekhoudt, L. *et al.* Chemogenetic activation of dopamine neurons in the ventral tegmental area, but not substantia nigra, induces hyperactivity in rats. *Eur. Neuropsychopharmacol.* **26**, 1784–1793 (2016).

34. Jing, M. Y. *et al.* Re-examining the role of ventral tegmental area dopaminergic neurons in motor activity and reinforcement by chemogenetic and optogenetic manipulation in mice. *Metab. Brain Dis.* **34**, 1421–1430 (2019).

35. Nagai, J. *et al.* Behaviorally consequential astrocytic regulation of neural circuits. *Neuron* 1–21 (2021) doi:10.1016/j.neuron.2020.12.008.

908 36. Kofuji, P. & Araque, A. Astrocytes and Behavior. *Annu. Rev. Neurosci.* **44**, 49–67
909 (2021).
910 37. Martin-Fernandez, M. *et al.* Synapse-specific astrocyte gating of amygdala-related
911 behavior. *Nat. Neurosci.* **20**, (2017).
912 38. Adamsky, A. *et al.* Astrocytic Activation Generates De Novo Neuronal Potentiation
913 and Memory Enhancement. *Cell* **174**, 59-71.e14 (2018).
914 39. Min, R. & Nevian, T. Astrocyte signaling controls spike timing-dependent depression
915 at neocortical synapses. *Nat. Neurosci.* **15**, (2012).
916 40. Nagai, J. *et al.* Hyperactivity with Disrupted Attention by Activation of an Astrocyte
917 Synaptogenic Cue. *Cell* **177**, 1280-1292.e20 (2019).
918 41. Jennings, A. *et al.* Dopamine elevates and lowers astroglial Ca2+ through distinct
919 pathways depending on local synaptic circuitry. *Glia* **65**, 447–459 (2017).
920 42. Xin, W. *et al.* Ventral midbrain astrocytes display unique physiological features and
921 sensitivity to dopamine D2 receptor signaling. *Neuropsychopharmacology* **44**, 344–
922 355 (2019).
923 43. Cui, Q. *et al.* Blunted mGluR Activation Disinhibits Striatopallidal Transmission in
924 Parkinsonian Mice. *Cell Rep.* **17**, 2431–2444 (2016).
925 44. Corkrum, M. *et al.* Dopamine-Evoked Synaptic Regulation in the Nucleus Accumbens
926 Requires Astrocyte Activity. *Neuron* **105**, (2020).
927 45. Fuxe, K., Agnati, L. F., Marcoli, M. & Borroto-Escuela, D. O. Volume Transmission in
928 Central Dopamine and Noradrenaline Neurons and Its Astroglial Targets. *Neurochem.*
929 *Res.* **40**, 2600–2614 (2015).
930 46. Kearn, C. S., Blake-Palmer, K., Daniel, E., Mackie, K. & Glass, M. Concurrent
931 stimulation of cannabinoid CB1 and dopamine D2 receptors enhances heterodimer
932 formation: a mechanism for receptor cross-talk? *Mol. Pharmacol.* **67**, 1697–1704
933 (2005).

934 47. Mariotti, L. *et al.* Interneuron-specific signaling evokes distinctive somatostatin-
935 mediated responses in adult cortical astrocytes. *Nat. Commun.* **9**, (2018).
936 48. Shigetomi, E., Jackson-Weaver, O., Huckstepp, R. T., O'Dell, T. J. & Khakh, B. S.
937 TRPA1 Channels Are Regulators of Astrocyte Basal Calcium Levels and Long-Term
938 Potentiation via Constitutive D-Serine Release. *J. Neurosci.* **33**, 10143–10153 (2013).
939 49. Engelhard, B. *et al.* Specialized coding of sensory, motor and cognitive variables in
940 VTA dopamine neurons. *Nature* **570**, 509–513 (2019).
941 50. Li, X., Zima, A. V., Sheikh, F., Blatter, L. A. & Chen, J. Endothelin-1-induced
942 arrhythmogenic Ca2+ signaling is abolished in atrial myocytes of inositol-1,4,5-
943 trisphosphate(IP3)-receptor type 2-deficient mice. *Circ. Res.* **96**, 1274–1281 (2005).
944 51. Marsicano, G. *et al.* The endogenous cannabinoid system controls extinction of
945 aversive memories. *Nature* **418**, 530–534 (2002).
946 52. Bello, E. P. *et al.* Cocaine supersensitivity and enhanced motivation for reward in mice
947 lacking dopamine D2 autoreceptors. *Nat. Neurosci.* **14**, 1033–1038 (2011).
948 53. Dugué, G. P., Dumoulin, A., Triller, A. & Dieudonné, S. Target-dependent use of
949 coreleased inhibitory transmitters at central synapses. *J. Neurosci.* **25**, 6490–6498
950 (2005).
951 54. Bellone, C., Mameli, M. & Lüscher, C. In utero exposure to cocaine delays postnatal
952 synaptic maturation of glutamatergic transmission in the VTA. *Nat. Neurosci.* **14**,
953 1439–1446 (2011).
954 55. Chieng, B., Azriel, Y., Mohammadi, S. & Christie, M. J. Distinct cellular properties of
955 identified dopaminergic and GABAergic neurons in the mouse ventral tegmental area.
956 *J. Physiol.* **589**, 3775–3787 (2011).
957 56. Melone, M., Bellesi, M. & Conti, F. Synaptic localization of GLT-1a in the rat somatic
958 sensory cortex. *Glia* **57**, 108–117 (2009).
959 57. Murphy, M. J. M. & Deutch, A. Y. Organization of afferents to the orbitofrontal cortex

960 in the rat. *J. Comp. Neurol.* **526**, 1498–1526 (2018).
961 58. Phend, K. D., Rustioni, A. & Weinberg, R. J. An osmium-free method of Epon
962 embedment that preserves both ultrastructure and antigenicity for post-embedding
963 immunocytochemistry. *J. Histochem. Cytochem.* **43**, 283–292 (1995).
964 59. Melone, M., Ciriachi, C., Pietrobon, D. & Conti, F. Heterogeneity of astrocytic and
965 neuronal GLT-1 at cortical excitatory synapses, as revealed by its colocalization with
966 Na+/K+-ATPase α isoforms. *Cereb. Cortex* **29**, 3331–3350 (2019).
967 60. Peters, A., Palay, S. L. & Webster, H. D. The fine structure of the nervous system:
968 The neurons and supporting cells, by Alan Peters, Sanford L. Palay, and Henry Def.
969 Webster, 395 pp, illustrated, $33.00, W. B. Saunders Company, Philadelphia, 1976.
970 *Ann. Neurol.* **4**, 588 (1978).
971 61. DeFelipe, J. Estimation of the number of synapses in the cerebral cortex:
972 Methodological considerations. *Cereb. Cortex* **9**, 722–732 (1999).
973 62. Hervé, D., Pickel, V. M., Joh, T. H. & Beaudet, A. Serotonin axon terminals in the
974 ventral tegmental area of the rat: fine structure and synaptic input to dopaminergic
975 neurons. *Brain Res.* **435**, 71–83 (1987).
976 63. Tamiya, R., Hanada, M., Kawai, Y., Inagaki, S. & Takagi, H. Substance P afferents
977 have synaptic contacts with dopaminergic neurons in the ventral tegmental area of
978 the rat. *Neurosci. Lett.* **110**, 11–15 (1990).
979 64. Tagliaferro, P. & Morales, M. Synapses between corticotropin-releasing factor-
980 containing axon terminals and dopaminergic neurons in the ventral tegmental area
981 are predominantly glutamatergic. *J. Comp. Neurol.* **506**, 616–626 (2008).
982 65. Racz, B. & Weinberg, R. J. The subcellular organization of cortactin in hippocampus.
983 *J. Neurosci.* **24**, 10310–10317 (2004).
984 66. Petrescu, A. D. *et al.* Physical and Functional Interaction of Acyl-CoA-binding Protein
985 with Hepatocyte Nuclear Factor-4α. *J. Biol. Chem.* **278**, 51813–51824 (2003).

986 67. Storey, S. M. *et al.* Loss of intracellular lipid binding proteins differentially impacts
987 saturated fatty acid uptake and nuclear targeting in mouse hepatocytes. *Am. J.*
988 *Physiol. - Gastrointest. Liver Physiol.* **303**, (2012).
989 68. Laffray, S. *et al.* Impairment of GABAB receptor dimer by endogenous 14-3-3 ζ in
990 chronic pain conditions. *EMBO J.* **31**, 3239–3251 (2012).
991 69. Amiry-Moghaddam, M. & Ottersen, O. P. Immunogold cytochemistry in neuroscience.
992 *Nat. Neurosci.* **16**, 798–804 (2013).
993 70. Ohtani, Y. *et al.* The synaptic targeting of mGluR1 by Its carboxyl-terminal domain is
994 crucial for cerebellar function. *J. Neurosci.* **34**, 2702–2712 (2014).
995 71. Garcia-Ovejero, D., Arevalo-Martin, A., Paniagua-Torija, B., Sierra-Palomares, Y. &
996 Molina-Holgado, E. A cell population that strongly expresses the CB1 cannabinoid
997 receptor in the ependyma of the rat spinal cord. *J. Comp. Neurol.* **521**, 233–251
998 (2013).
999 72. Stojanovic, T. *et al.* Validation of dopamine receptor DRD1 and DRD2 antibodies
1000 using receptor deficient mice. *Amino Acids* **49**, 1101–1109 (2017).
1001 73. Solís, O., Garcia-Montes, J. R., González-Granillo, A., Xu, M. & Moratalla, R.
1002 Dopamine D3 receptor Modulates l-DOPA-Induced Dyskinesia by Targeting D1
1003 Receptor-Mediated Striatal Signaling. *Cereb. Cortex* **27**, 435–446 (2017).
1004 74. Castro-Hernández, J. *et al.* Prolonged treatment with pramipexole promotes physical
1005 interaction of striatal dopamine D3 autoreceptors with dopamine transporters to
1006 reduce dopamine uptake. *Neurobiol. Dis.* **74**, 325–335 (2015).
1007 75. Barili, P., Bronzetti, E., Ricci, A., Zaccheo, D. & Amenta, F. Microanatomical
1008 localization of dopamine receptor protein immunoreactivity in the rat cerebellar cortex.
1009 *Brain Res.* **854**, 130–138 (2000).
1010 76. Grace, A. A. & Bunney, B. S. Intracellular and extracellular electrophysiology of nigral
1011 dopaminergic neurons—1. Identification and characterization. *Neuroscience* **10**, 301–

315 (1983).

77. Ungless, M. A., Magill, P. J. & Bolam, J. P. Uniform Inhibition of Dopamine Neurons in the Ventral Tegmental Area by Aversive Stimuli. *Science (80-.).* **303**, 2040–2042 (2004).

78. Ungless, M. A. & Grace, A. A. Are you or aren't you? Challenges associated with physiologically identifying dopamine neurons. *Trends Neurosci.* **35**, 422–430 (2012).

79. Lecca, S., Melis, M., Luchicchi, A., Muntoni, A. L. & Pistis, M. Inhibitory inputs from rostromedial tegmental neurons regulate spontaneous activity of midbrain dopamine cells and their responses to drugs of abuse. *Neuropsychopharmacology* **37**, 1164–1176 (2012).

80. Grace, A. A. & Bunney, B. S. The control of firing pattern in nigral dopamine neurons: Burst firing. *J. Neurosci.* **4**, 2877–2890 (1984).

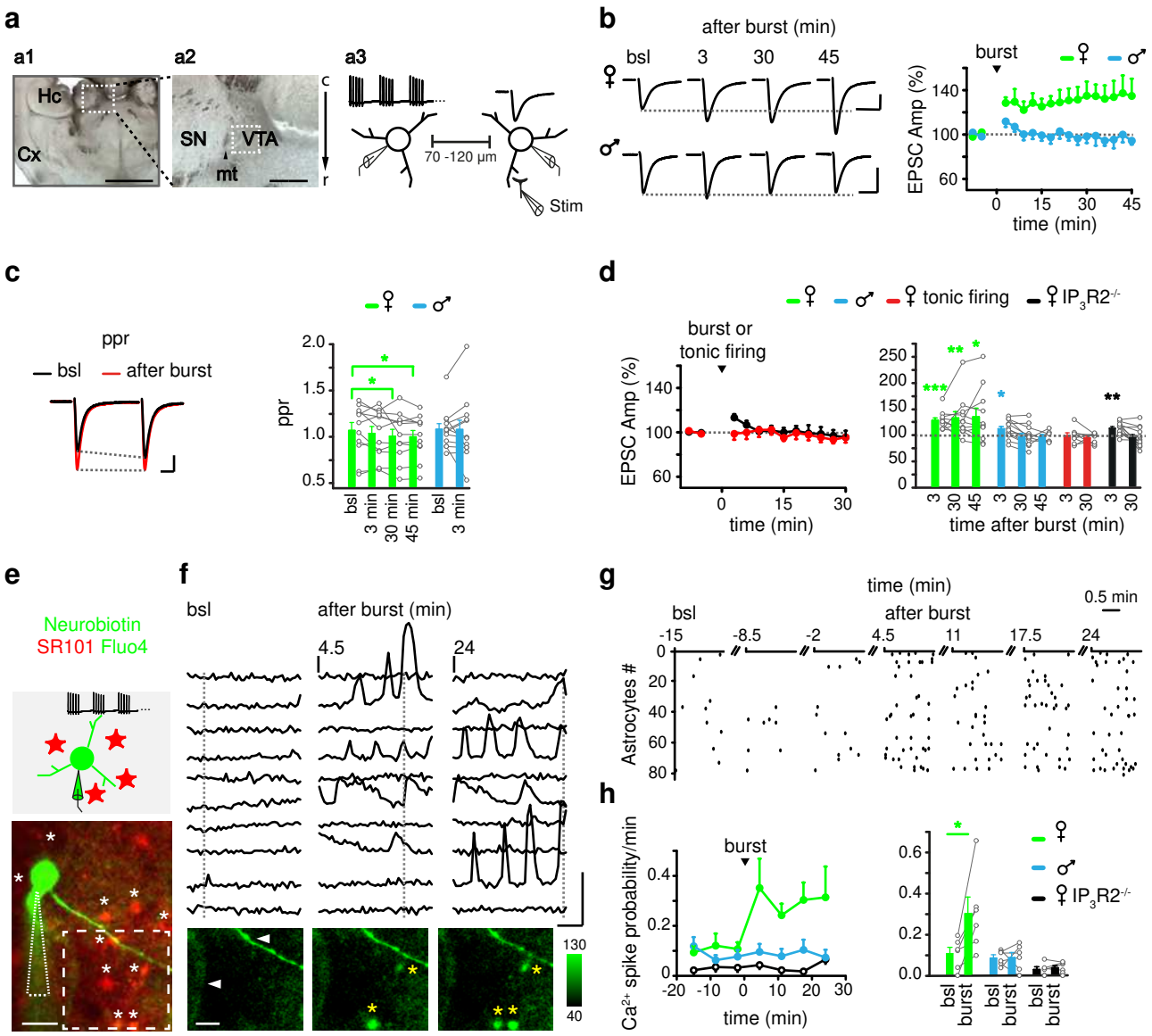

Figure 1. Astrocyte recruitment by DA neuron burst firing induces LTP of excitatory synapses onto adjacent DA neurons in young female mice. a) a1, low-magnification from a horizontal brain slice with a caudal-rostral orientation. Cx, cortex, Hc, hippocampus. Scale bar, 1 mm. a2, high magnification of the area indicated in a1. mt, medial terminal nucleus of the accessory optical tract; SN, substantia nigra (lateral to mt); VTA, ventral tegmental area (medial to mt), c, caudal; r, rostral. Dashed square, lateral part of the VTA where conventional DA neurons were recorded. Scale bar, 200 µm. a3, schematic of the experimental design showing a DA neuron pair, two recording pipettes, the burst firing imposed to a DA neuron (left) and the EPSC evoked on the other DA neuron (right) by extracellular stimulation of rostral glutamatergic afferents (Stim). b) Left, evoked EPSCs at basal conditions (bsl) and at different time points after bursts, from slices of female (upper traces) and male (lower traces) mice. Stimulus artifacts were removed. Scale bars, 50 pA, 20 ms. Right, EPSC amplitude in female (n = 11) and male (n ≥ 6) mice after the burst firing protocol (arrowhead). In this and the other figures reporting EPSC amplitude vs time, t = 0 indicates the end of the burst firing. c) Left, representative pair of evoked EPSCs (time interval, 50 ms) from a DA neuron of a female mouse, before (bsl, black traces) and after bursts (red traces). Scale bars, 20 pA, 10 ms. Right, paired-pulse ratio (ppr) values vs time in female (n = 11) and male (n = 12) mice. d) Left, EPSC amplitude after tonic and burst firing protocol in wt female mice (n = 8) and $IP_3R2^{-/-}$ female mice (n = 12), respectively. Right, EPSC amplitude at time points indicated after burst/tonic firing in the different groups. e) Schematic and fluorescence image of a neurobiotin-488 filled DA neuron (dotted line, patch pipette) and SR101-loaded astrocytes (white asterisks). Scale bar, 30 µm. **See next page.**

Figure 1. f) Upper panel, time course of Ca^{2+} levels from astrocytes shown in (e) at basal conditions, 4.5 min and 24 min after burst firing. Scale bars, 100 %, 20 s. Lower panel, Fluo-4 fluorescence images of the dashed square shown in e). Arrows, two DA neuron dendrites at different focal planes; yellow asterisks, astrocytes displaying Ca^{2+} transients (upper traces) at the time points indicated (dashed lines). Scale bar, 20 μm. g) Raster plot reporting the onset of Ca^{2+} transients from 84 astrocytes, at basal conditions and after DA neuron burst firing. In this and the other figures reporting the time course of the astrocytic Ca^{2+} spike probability/min, t = 0 indicates burst firing onset. h) Left, time course of astrocytic Ca^{2+} spike probability/min in female, male and $IP_3R2^{-/-}$ female mice (n = 6), before and after burst firing. Right, Ca^{2+} spike probability/min in basal conditions and after burst firing. In this and the other figures, data are represented as mean ± SEM; *, < 0.05; **, < 0.01; ***, <0.001; ****, < 0.0001.

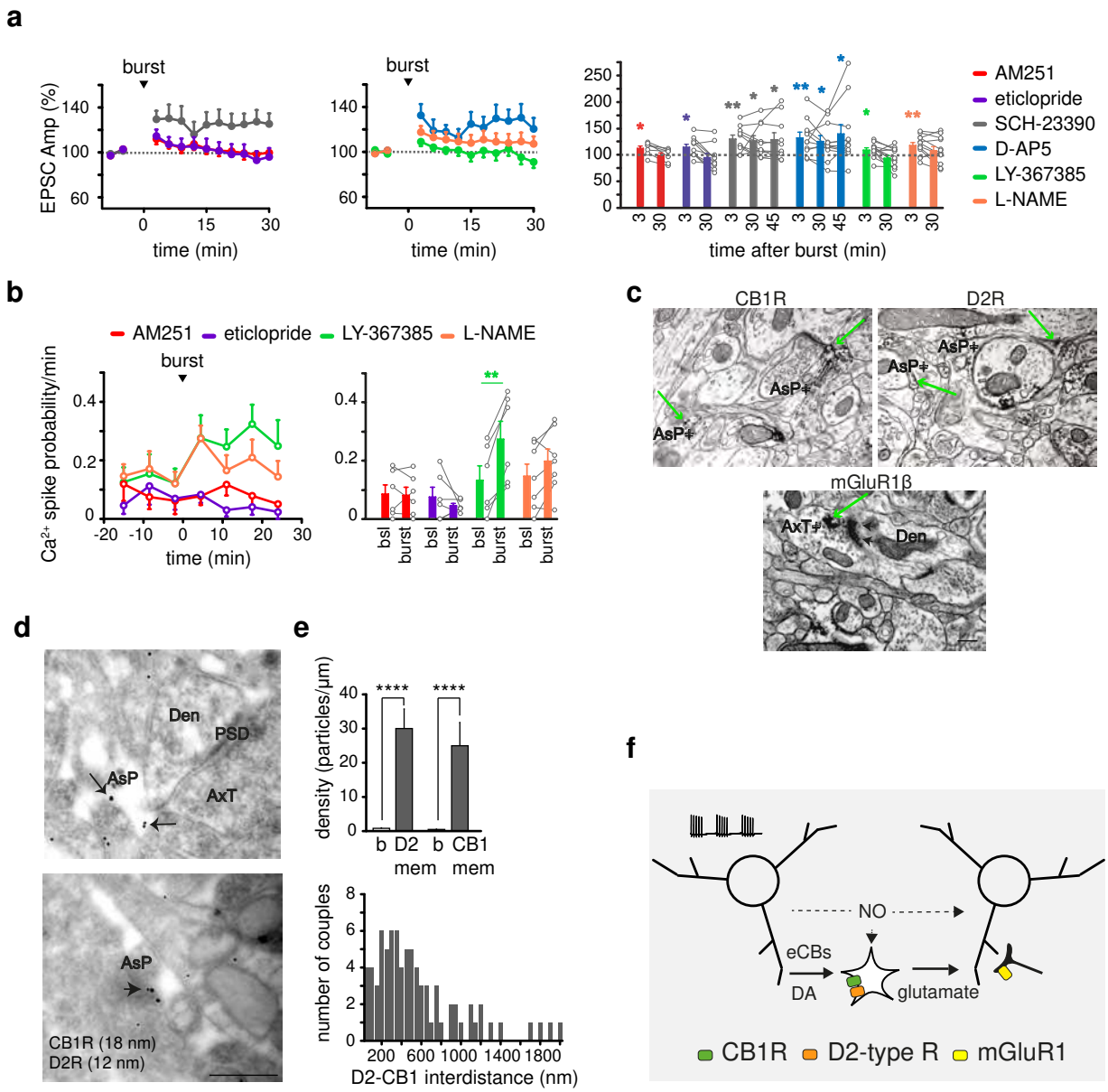

Figure 2. bLTP generation in female mice requires both eCB and DA signaling to astrocytes, mGluR1 activation and NO signaling. a) Time course and bar chart of EPSC amplitude in the presence of different antagonists (AM251 (CB1R), n = 7; eticlopride (D2-type R), n = 10; SCH-23390 (D1-type R), n = 10; D-AP5 (NMDAR), n = 11; LY-367385 (mGluR1), n = 12; L-NAME (NO synthase), n = 12). b) Time course and bar chart of astrocytic Ca^{2+} spike probability/min in the presence of antagonists that impaired bLTP generation (n ≥ 6). c) Pre-embedding electron microscopy images from lateral VTA of a young female mouse of CB1, D2 and mGluR1β receptors. Green arrows, immunopositive products in AsP (AsP+) and AxT (AxT+) forming asymmetric synaptic contacts (arrowheads) with a dendrite (Den). Scale bar, 300 nm. d) Post-embedding electron microscopy images of CB1/D2R immunogold double-labelled astrocytic processes (AsP) in lateral VTA (CB1R, 18 nm gold particles; D2R, 12 nm gold particles). Upper panel, a double-labelled AsP expressing CB1 and D2R (arrows) in close apposition to an asymmetric synapse (AxT, axon terminal; Den, dendrite; PSD, post-synaptic density). Lower panel, an edge-to-edge separation distance between these receptors ≤ 50 nm (arrowhead. Scale bar, 300 nm. e) Upper panel, CB1 and D2R immunogold densities at the membranes of astrocytic processes (AsP, n = 79 from two P16 females; 30.1 ± 2.6 gold particles/µm^2 for D2Rs (D2 mem), and 24.9 ± 2.0 particles/µm^2 for CB1Rs (CB1 mem)) and at neuronal nuclei (b, background values, n = 10; 0.82 ± 0.12 for 12 nm gold particles; 0.49 ± 0.07 for 18 nm gold particles, Mann-Whitney test). Lower panel, distribution of the edge-to-edge interdistances (bin, 50 nm) between membrane D2 and CB1R immunogold couples. f) Schematic of the proposed cellular and molecular mechanism for bLTP generation (see text for details).

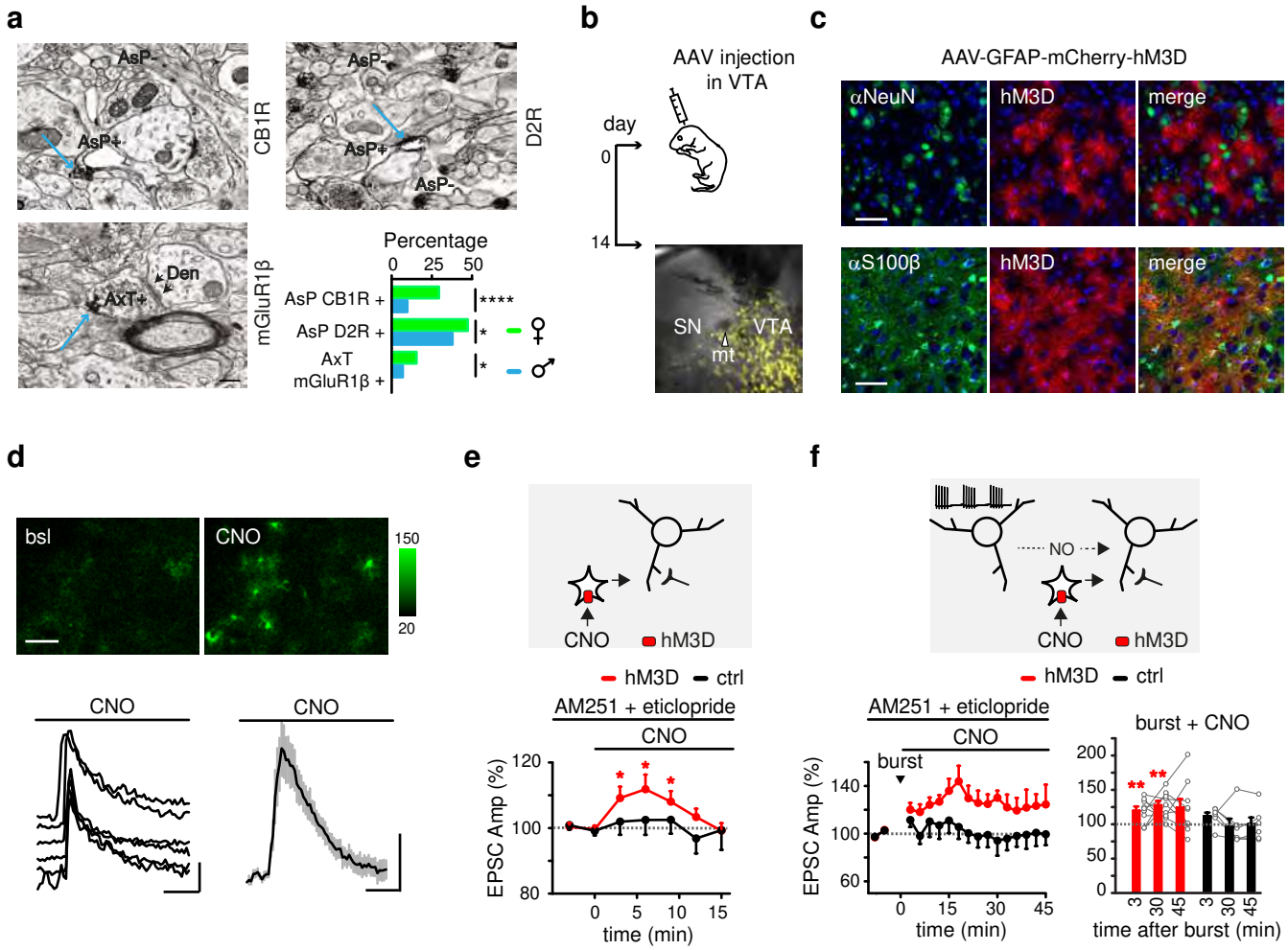

Figure 3. **Chemogenetic selective activation of astrocytes rescues bLTP in young male mice.** a) Representative pre-embedding electron microscopy in the lateral VTA from a young male mouse of CB1 and D2R expression at AsP and mGlurR1β expression at AxT forming asymmetric synaptic contact (arrowheads) with dendrite (Den). Blue arrows, immunopositive products in AsP (AsP+) and AxT. AsP-, AsP without immunoreactivity. Scale bar, 300 nm. Lower panel, quantification and comparison (contingency Fisher's test) of CB1, D2 and mGlu1βR expression in female and male mice. b) Schematic of the AAV-9/2-hGFAP-hM3D(Gq)_mCherry-WPRE-hGHp(A) injection in the VTA of a neonatal male mouse and fluorescence image of a brain slice two weeks after injection (yellow, mCherry-hM3D expression). c) Confocal images of the VTA from a mouse injected with AAV-9/2-hGFAP-hM3D(Gq)_mCherry-WPRE-hGHp(A), showing the fluorescence of mCherry-hM3D (red), the nuclear Top-Ro3 (blue) and the specific green fluorescence for either neurons (α-NeuN staining) or astrocytes (α-S100β staining). Scale bars, 50 µm. d) GCaMP6f fluorescence images of astrocytes in basal conditions and after CNO perfusion. Scale bar, 50 µm. Lower panels, time course of Ca^{2+} elevations evoked by CNO in these astrocytes (scale bars, 100%, 30 s) and mean change of total Ca^{2+} levels in slices (n = 9) expressing GCaMP6f and hM3D in astrocytes in response to CNO (scale bars, 2%, 30 s). e) Upper panel, schematic of the experimental design. Lower panel, CNO transiently increases EPSC amplitude of DA neurons in male mice expressing hM3D in astrocytes (n = 9), but not in non-injected mice (n = 8). These experiments were performed in the presence of AM251 and eticlopride. f) Upper panel, schematic of the experimental design. Lower panel, pairing of burst firing protocol and CNO application partially rescues bLTP in male mice expressing hM3D in astrocytes (n = 9), but not in non-injected mice (n = 6). These experiments were performed in the presence of AM251 and eticlopride.

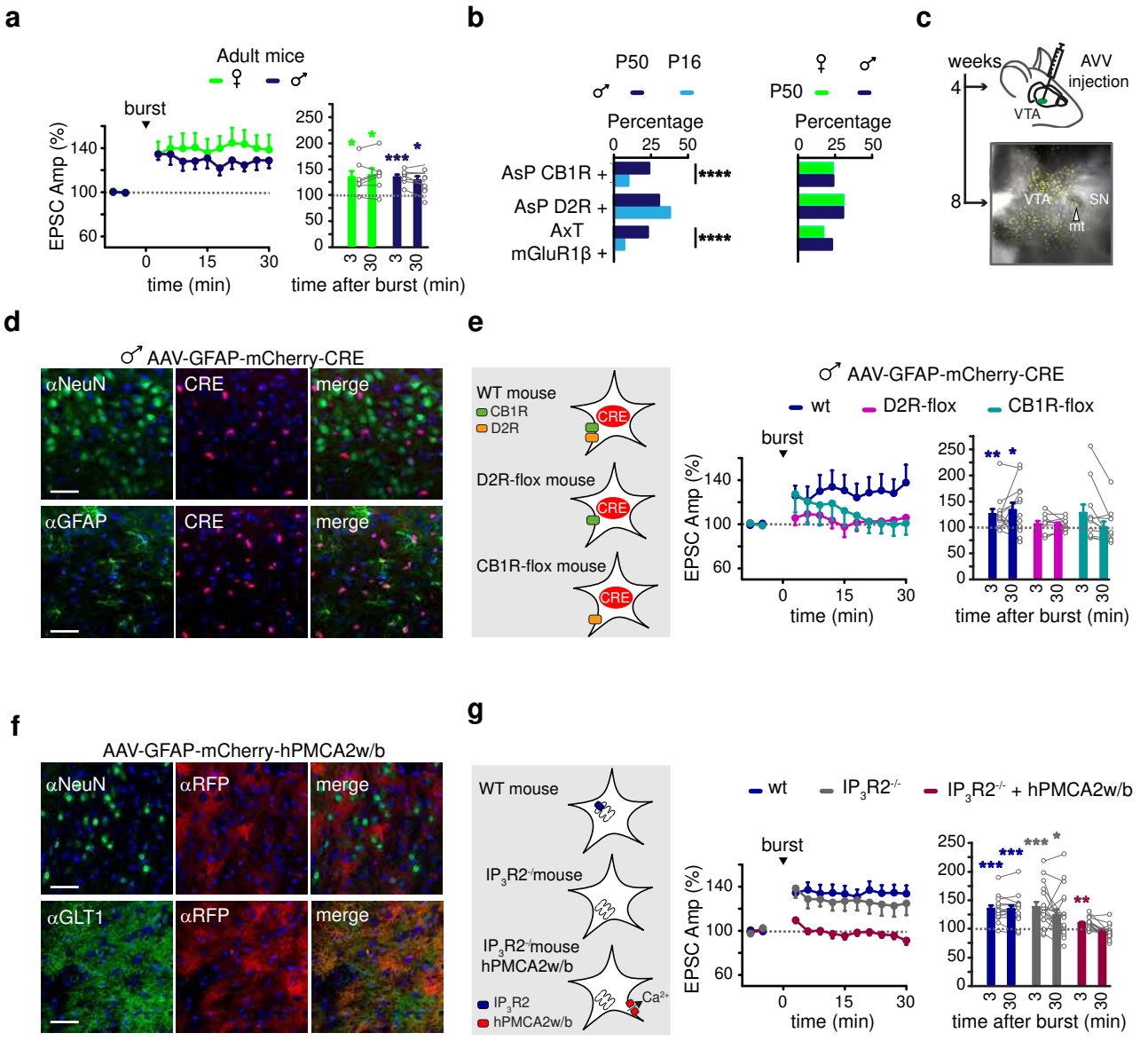

Figure 4. Astrocytes induce bLTP in both female and male adult mice and bLTP is abolished in adult IP$_3$R2$^{-/-}$ mice expressing a plasmatic Ca^{2+} pump in astrocytes. a) The bLTP is present in both female (n = 7) and male (n = 7) adult mice. b) Quantification and comparison (contingency Fisher's test) of CB1, D2 and mGluR1β receptors expression in young and adult male mice and in adult female and male mice. c) Schematic of the AAV9-hGFAP-mCherry_iCre-WPRE-hGHp(A) injection in adult male mouse VTA and fluorescence image of a brain slice four weeks after viral injection (yellow, mCherry-Cre expression). d) Confocal images of the VTA from an adult male mouse injected with AAV9-hGFAP-mCherry_iCre-WPRE-hGHp(A), showing the fluorescence of mCherry-Cre (red), the nuclear Top-Ro3 (blue) and the specific green fluorescence for either neurons (α-NeuN staining) or astrocytes (α-GFAP staining). Scale bars, 50 µm. e) When male mice express the Cre recombinase in VTA astrocytes, bLTP is preserved in wt mice (n = 13), but abolished in D2R- (n = 9) or CB1R-Floxed (n = 11) mice. f) Confocal images of the VTA from an adult IP$_3$R2$^{-/-}$ mouse injected with AAV5-GfaABC1D-mCherry-hPMCA2w/b.SV40, showing the expression of the Ca^{2+} pump hPMCA2w/b (α-RFP red staining), the blue nuclear Top-Ro3 staining and specific green staining for either neurons (α-NeuN staining) or astrocytes (α-GLT1 staining). Scale bars, 50 µm. g) In adult mice the bLTP is abolished in IP$_3$R2$^{-/-}$ mice expressing the Ca^{2+} pump hPMCA2w/b in astrocytes (n = 14).

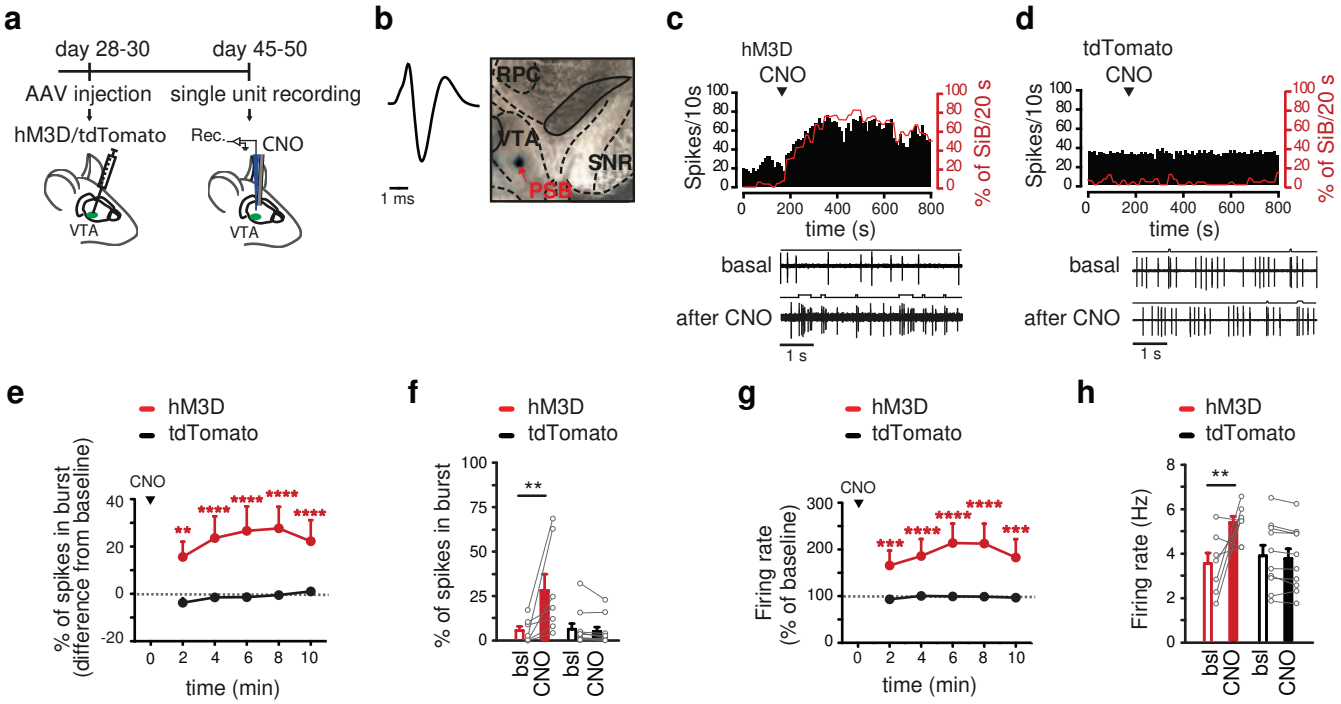

Figure 5. Chemogenetic activation of astrocytes *in vivo* favors bursting and overall firing activity in VTA DA neurons. a) Schematic of the experimental design showing the pipettes for recording (blue) and CNO application (gray). b) Left, representative action potential (start to end > 2.5 ms) from a putative VTA DA neuron. Right, location of a recorded putative VTA DA neuron. PSB; pontamine sky blue; SNR, susbtantia nigra pars reticulata; RPC, red nucleus. c, d) Upper panels, representative firing rate (Spikes/10 s) histograms and percentage of spikes in burst (SiB/20 s) trends over time of VTA DA neurons from mice expressing hM3D (c) or tdTomato (d) in VTA astrocytes. Lower panel, examples of raw spike traces of the same neurons before and after local CNO applications. e) Time course of the bursting activity (after local CNO applications (hM3D, n = 7; tdTomato n = 10). Two-way RM ANOVA and Bonferroni's multiple comparison test: main effects are not indicated; hM3D 2 minutes vs. hM3D basal **p < 0.01; hM3D 4, 6, 8, 10 minutes vs. hM3D basal **** p < 0.0001. f) Percentage of spikes in bursts before and after local CNO applications (n hM3D = 7; n tdTtomato = 10). Two-way RM ANOVA and Bonferroni's multiple comparison test: main effects are not indicated; hM3D after CNO vs. hM3D basal ** p < 0.01. g) Time course of the firing rate after local CNO applications (hM3D, n = 7; tdTomato, n = 10). Two-way RM ANOVA and Bonferroni's multiple comparison test: main effects are not indicated; hM3D 2, 10 minutes vs. hM3D basal ***p < 0.001; hM3D 4, 6, 8 minutes vs. hM3D basal **** p < 0.0001. h) Firing rate before and after local CNO applications. Two-way RM ANOVA and Bonferroni's multiple comparison test: main effects are not indicated; hM3D after CNO vs. hM3D basal ** p < 0.01.

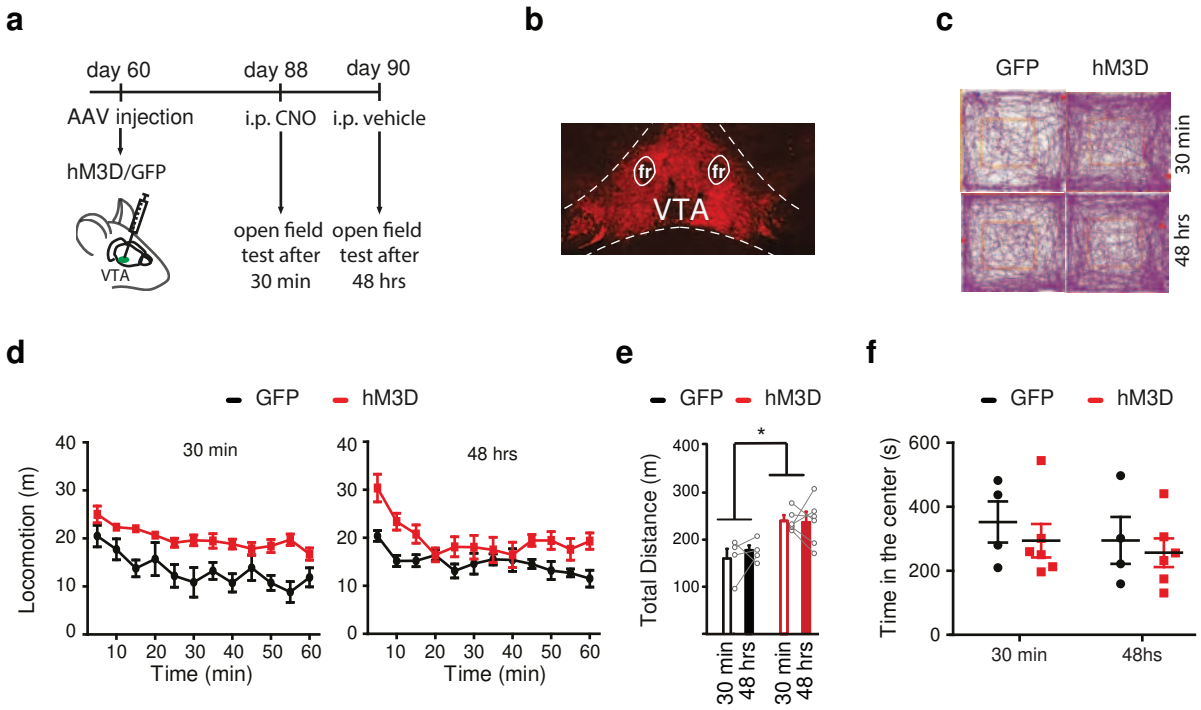

Figure 6. Chemogenetic activation of astrocytes *in vivo* induces a long-lasting motor hyperactivity. a) Schematic of the experimental design for testing locomotion in mice expressing in VTA astrocytes either GFP or hM3D, 30 min and 48 hrs after the intraperitoneal CNO application (3mg/kg). b) Fluorescence image of hM3D expression in VTA; fr, fasciculus retroflexus. c) Representative examples of locomotion in the open field test. d, e) Locomotor activity (d) and total distance (e) traveled by GFP- and hM3D-injected mice 30 min or 48 hrs after the intraperitoneal CNO injection (3 mg/kg, n = 4-6 mice/group). f) Time spent in the open field center of GFP- and hM3D-injected mice, at different time points after the intraperitoneal CNO injection.

Figures

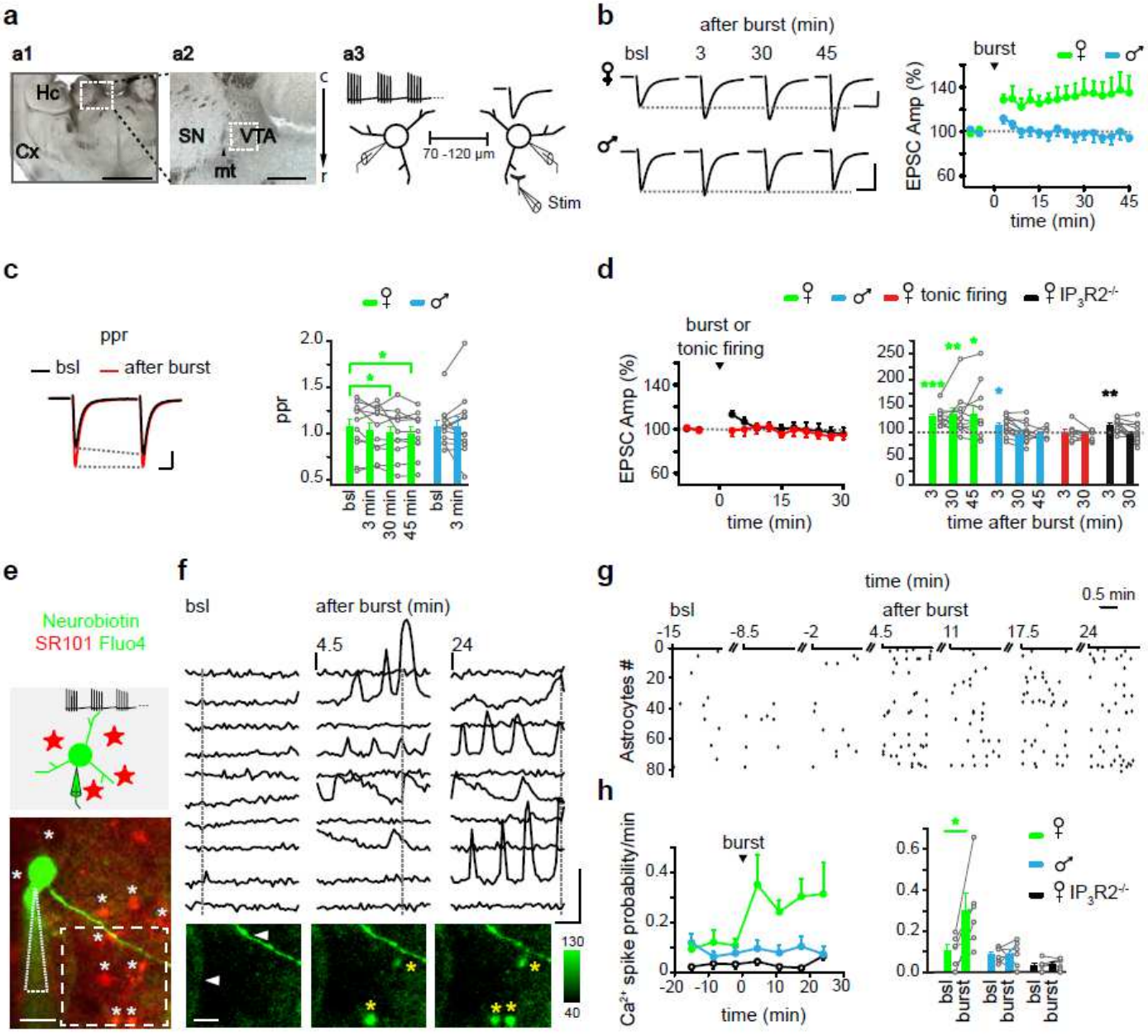

Figure 1

Astrocyte recruitment by DA neuron burst firing induces LTP of excitatory synapses onto adjacent DA neurons in young female mice. a) a1, low-magnification from a horizontal brain slice with a caudal-rostral orientation. Cx, cortex, Hc, hippocampus. Scale bar, 1 mm. a2, high magnification of the area indicated in a1. mt, medial terminal nucleus of the accessory optical tract; SN, substantia nigra (lateral to mt); VTA, ventral tegmental area (medial to mt), c, caudal; r, rostral. Dashed square, lateral part of the VTA where conventional DA neurons were recorded. Scale bar, 200 µm. a3, schematic of the experimental design showing a DA neuron pair, two recording pipettes, the burst firing imposed to a DA neuron (left) and the EPSC evoked on the other DA neuron (right) by extracellular stimulation of rostral glutamatergic afferents

(Stim). b) Left, evoked EPSCs at basal conditions (bsl) and at different time points after bursts, from slices of female (upper traces) and male (lower traces) mice. Stimulus artifacts were removed. Scale bars, 50 pA, 20 ms. Right, EPSC amplitude in female (n = 11) and male (n ≥ 6) mice after the burst firing protocol (arrowhead). In this and the other figures reporting EPSC amplitude vs time, t = 0 indicates the end of the burst firing. c) Left, representative pair of evoked EPSCs (time interval, 50 ms) from a DA neuron of a female mouse, before (bsl, black traces) and after bursts (red traces). Scale bars, 20 pA, 10 ms. Right, paired-pulse ratio (ppr) values vs time in female (n = 11) and male (n = 12) mice. d) Left, EPSC amplitude after tonic and burst firing protocol in wt female mice (n = 8) and IP3R2-/- female mice (n = 12), respectively. Right, EPSC amplitude at time points indicated after burst/tonic firing in the different groups. e) Schematic and fluorescence image of a neurobiotin-488 filled DA neuron (dotted line, patch pipette) and SR101-loaded astrocytes (white asterisks). Scale bar, 30 μm. f) Upper panel, time course of Ca^{2+} levels from astrocytes shown in (e) at basal conditions, 4.5 min and 24 min after burst firing. Scale bars, 100 %, 20 s. Lower panel, Fluo- 4 fluorescence images of the dashed square shown in e). Arrows, two DA neuron dendrites at different focal planes; yellow asterisks, astrocytes displaying Ca^{2+} transients (upper traces) at the time points indicated (dashed lines). Scale bar, 20 μm. g) Raster plot reporting the onset of Ca^{2+} transients from 84 astrocytes, at basal conditions and after DA neuron burst firing. In this and the other figures reporting the time course of the astrocytic Ca^{2+} spike probability/min, t = 0 indicates burst firing onset. h) Left, time course of astrocytic Ca^{2+} spike probability/min in female, male and IP3R2-/- female mice (n = 6), before and after burst firing. Right, Ca^{2+} spike probability/min in basal conditions and after burst firing. In this and the other figures, data are represented as mean ± SEM; *, < 0.05; **, < 0.01; ***, <0.001; ****, < 0.0001.

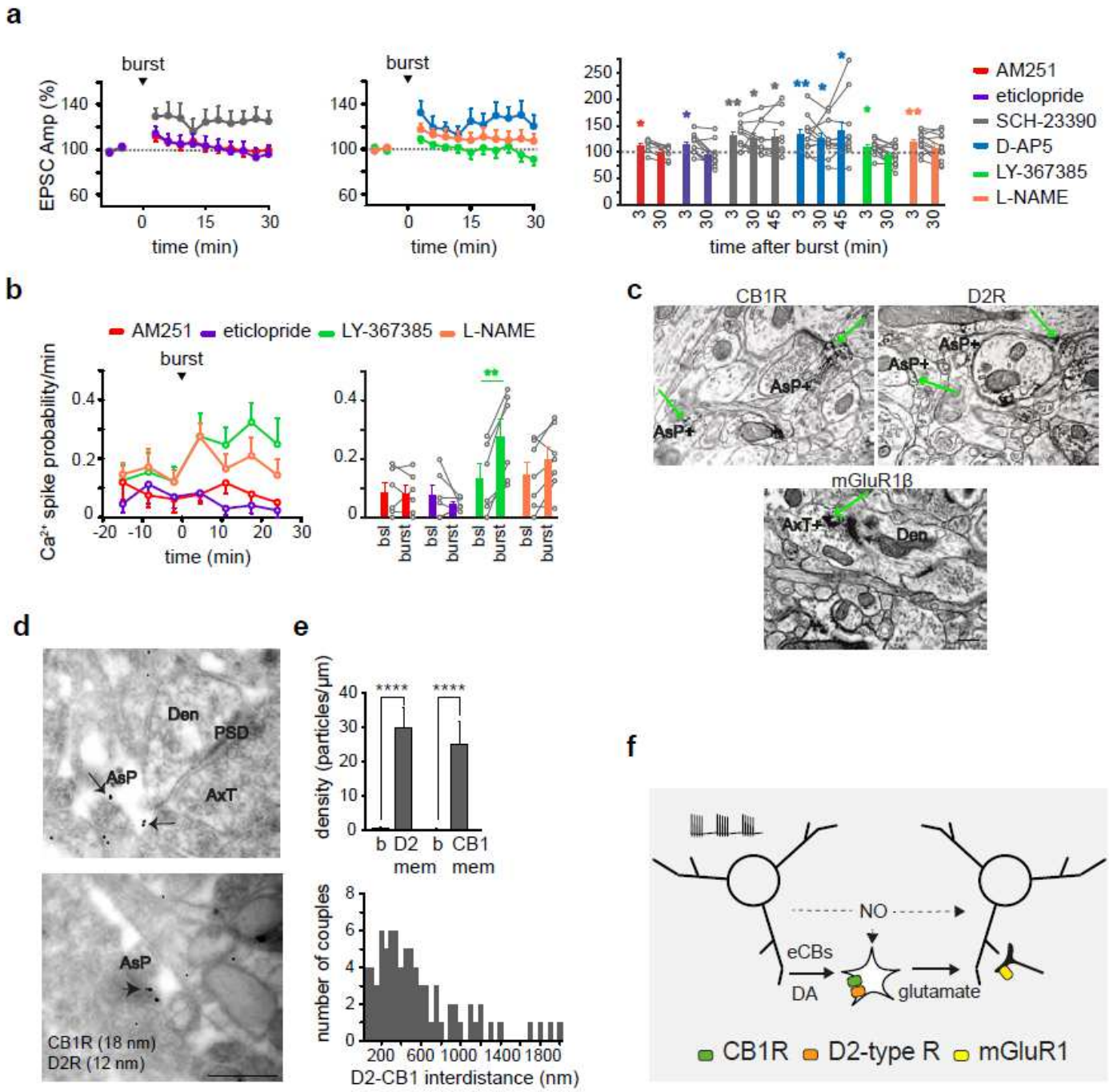

Figure 2

bLTP generation in female mice requires both eCB and DA signaling to astrocytes, mGluR1 activation and NO signaling. a) Time course and bar chart of EPSC amplitude in the presence of different antagonists (AM251 (CB1R), n = 7; eticlopride (D2- type R), n = 10; SCH-23390 (D1-type R), n = 10; D-AP5 (NMDAR), n = 11; LY-367385 (mGluR1), n = 12; L-NAME (NO synthase), n = 12). b) Time course and bar chart of astrocytic Ca2+ spike probability/min in the presence of antagonists that impaired bLTP generation (n ≥ 6). c) Pre-embedding electron microscopy images from lateral VTA of a young female mouse of CB1, D2 and mGluR1β receptors. Green arrows, immunopositive products in AsP (AsP+) and AxT (AxT+) forming asymmetric synaptic contacts (arrowheads) with a dendrite (Den). Scale bar, 300 nm. d) Post-embedding electron microscopy images of CB1/D2R immunogold double-labelled astrocytic processes (AsP) in

lateral VTA (CB1R, 18 nm gold particles; D2R, 12 nm gold particles). Upper panel, a double-labelled AsP expressing CB1 and D2R (arrows) in close apposition to an asymmetric synapse (AxT, axon terminal; Den, dendrite; PSD, post-synaptic density). Lower panel, an edge-to-edge separation distance between these receptors ≤ 50 nm (arrowhead. Scale bar, 300 nm. e) Upper panel, CB1 and D2R immunogold densities at the membranes of astrocytic processes (AsP, n = 79 from two P16 females; 30.1 ± 2.6 gold particles/µm2 for D2Rs (D2 mem), and 24.9 ± 2.0 particles/µm2 for CB1Rs (CB1 mem)) and at neuronal nuclei (b, background values, n = 10; 0.82 ± 0.12 for 12 nm gold particles; 0.49 ± 0.07 for 18 nm gold particles, Mann-Whitney test). Lower panel, distribution of the edge-to-edge interdistances (bin, 50 nm) between membrane D2 and CB1R immunogold couples. f) Schematic of the proposed cellular and molecular mechanism for bLTP generation (see text for details).

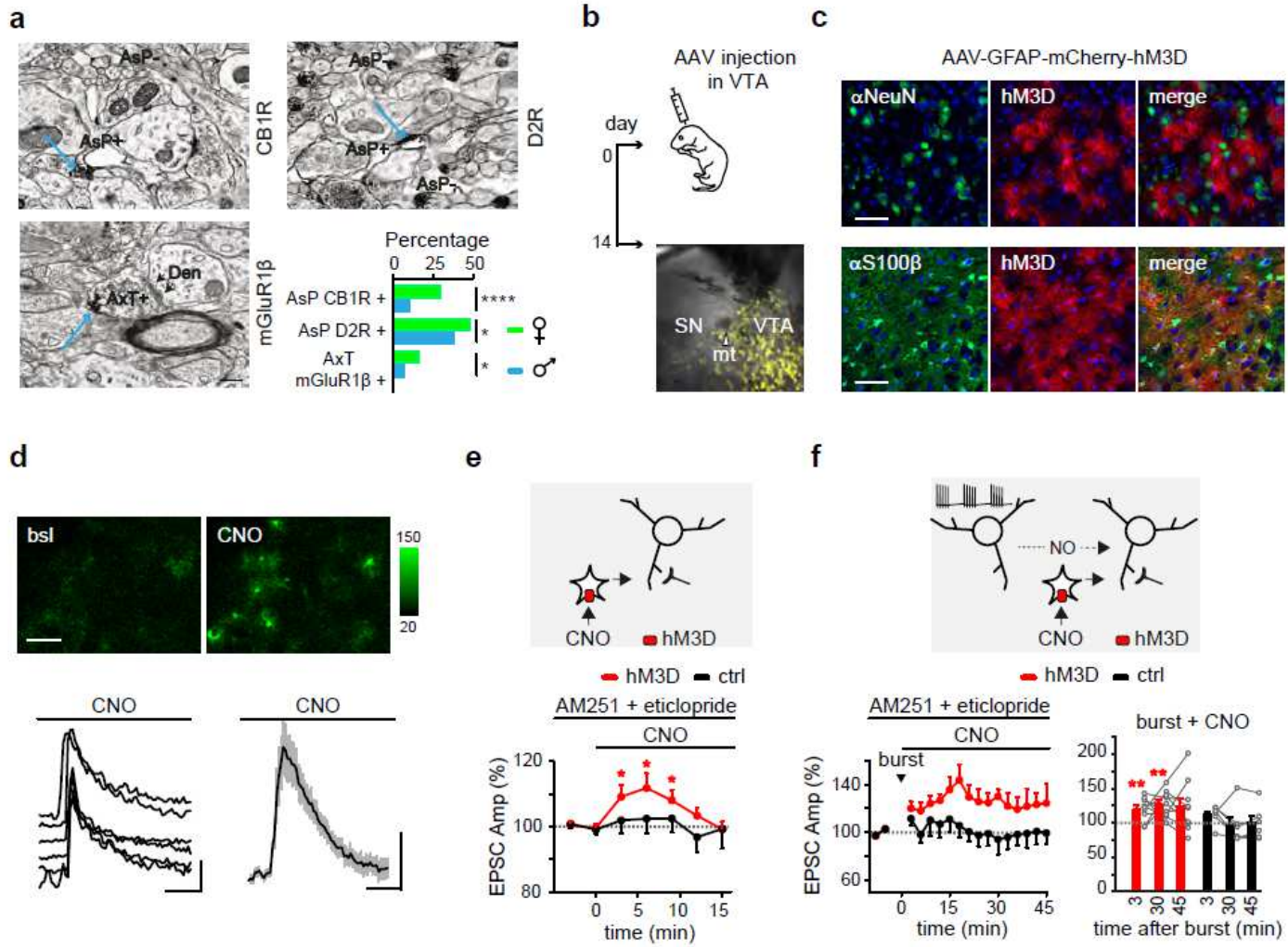

Figure 3

Chemogenetic selective activation of astrocytes rescues bLTP in young male mice. a) Representative pre-embedding electron microscopy in the lateral VTA from a young male mouse of CB1 and D2R expression at AsP and mGlurR1β expression at AxT forming asymmetric synaptic contact (arrowheads) with dendrite (Den). Blue arrows, immunopositive products in AsP (AsP+) and AxT. AsP-, AsP without immunoreactivity. Scale bar, 300 nm. Lower panel, quantification and comparison (contingency Fisher's

test) of CB1, D2 and mGlu1βR expression in female and male mice. b) Schematic of the AAV- 9/2-hGFAP-hM3D(Gq)_mCherry-WPRE-hGHp(A) injection in the VTA of a neonatal male mouse and fluorescence image of a brain slice two weeks after injection (yellow, mCherryhM3D expression). c) Confocal images of the VTA from a mouse injected with AAV-9/2- hGFAP-hM3D(Gq)_mCherry-WPRE-hGHp(A), showing the fluorescence of mCherry-hM3D (red), the nuclear Top-Ro3 (blue) and the specific green fluorescence for either neurons (α- NeuN staining) or astrocytes (α-S100β staining). Scale bars, 50 μm. d) GCaMP6f fluorescence images of astrocytes in basal conditions and after CNO perfusion. Scale bar, 50 μm. Lower panels, time course of Ca2+ elevations evoked by CNO in these astrocytes (scale bars, 100%, 30 s) and mean change of total Ca2+ levels in slices (n = 9) expressing GCaMP6f and hM3D in astrocytes in response to CNO (scale bars, 2%, 30 s). e) Upper panel, schematic of the experimental design. Lower panel, CNO transiently increases EPSC amplitude of DA neurons in male mice expressing hM3D in astrocytes (n = 9), but not in non-injected mice (n = 8). These experiments were performed in the presence of AM251 and eticlopride. f) Upper panel, schematic of the experimental design. Lower panel, pairing of burst firing protocol and CNO application partially rescues bLTP in male mice expressing hM3D in astrocytes (n = 9), but not in non-injected mice (n = 6). These experiments were performed in the presence of AM251 and eticlopride.

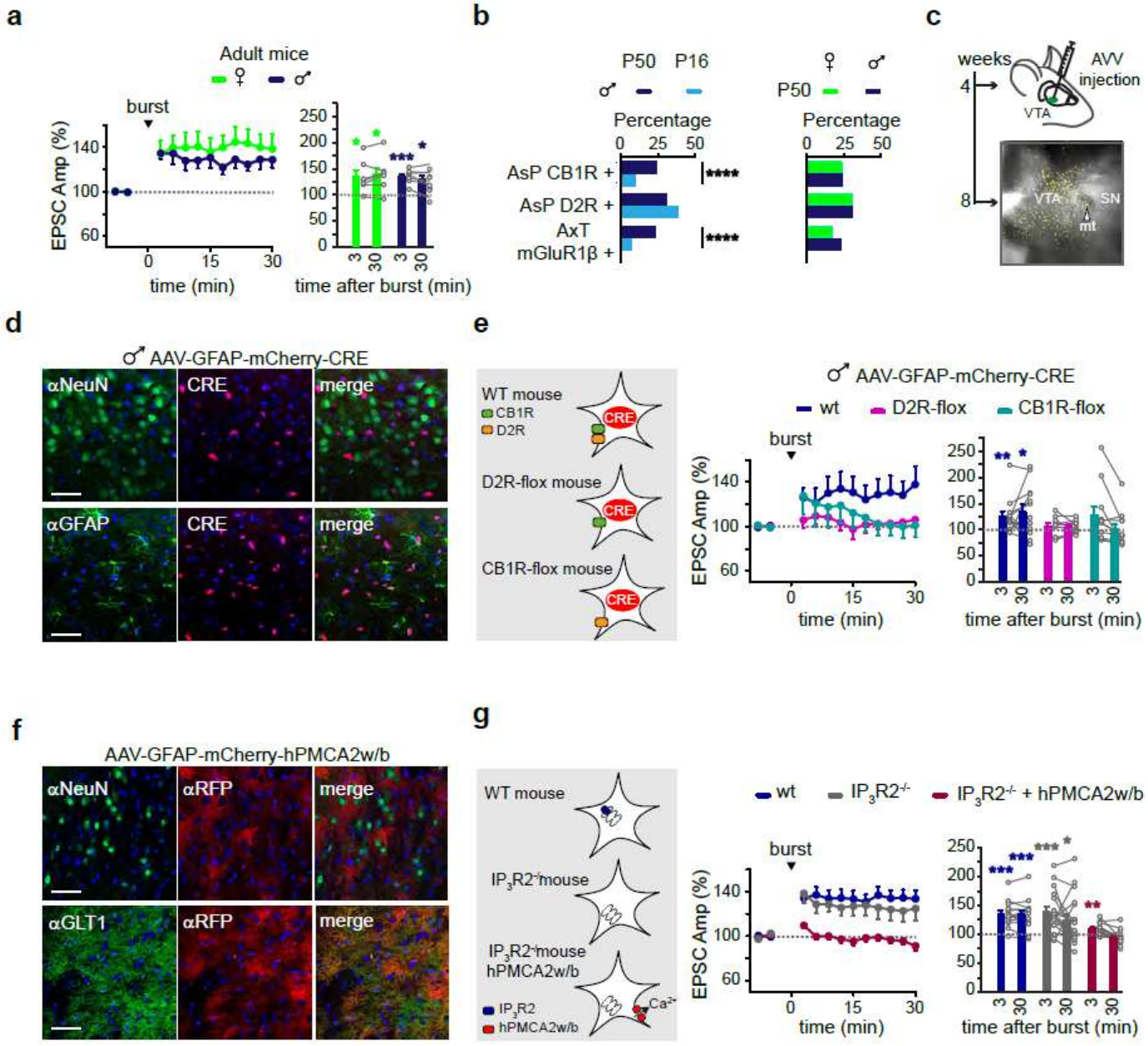

Figure 4

Astrocytes induce bLTP in both female and male adult mice and bLTP is abolished in adult IP3R2-/- mice expressing a plasmatic Ca2+ pump in astrocytes. a) The bLTP is present in both female (n = 7) and male (n = 7) adult mice. b) Quantification and comparison (contingency Fisher's test) of CB1, D2 and mGluR1β receptors expression in young and adult male mice and in adult female and male mice. c) Schematic of the AAV9- hGFAP-mCherry_iCre-WPRE-hGHp(A) injection in adult male mouse VTA and fluorescence image of a brain slice four weeks after viral injection (yellow, mCherry-Cre expression). d) Confocal images of the VTA from an adult male mouse injected with AAV9- hGFAP-mCherry_iCre-WPRE-hGHp(A), showing the fluorescence of mCherry-Cre (red), the nuclear Top-Ro3 (blue) and the specific green fluorescence for either neurons (α-NeuN staining) or astrocytes (α-GFAP staining). Scale bars, 50 µm. e) When male mice express the Cre recombinase in VTA astrocytes, bLTP is preserved in wt mice (n = 13), but abolished in D2R- (n = 9) or CB1R-Floxed (n = 11) mice. f) Confocal images of the VTA from an adult

IP3R2-/- mouse injected with AAV5-GfaABC1D-mCherry-hPMCA2w/b.SV40, showing the expression of the Ca2+ pump hPMCA2w/b (α-RFP red staining), the blue nuclear Top-Ro3 staining and specific green staining for either neurons (α-NeuN staining) or astrocytes (α- GLT1 staining). Scale bars, 50 μm. g) In adult mice the bLTP is abolished in IP3R2-/- mice expressing the Ca2+ pump hPMCA2w/b in astrocytes (n = 14).

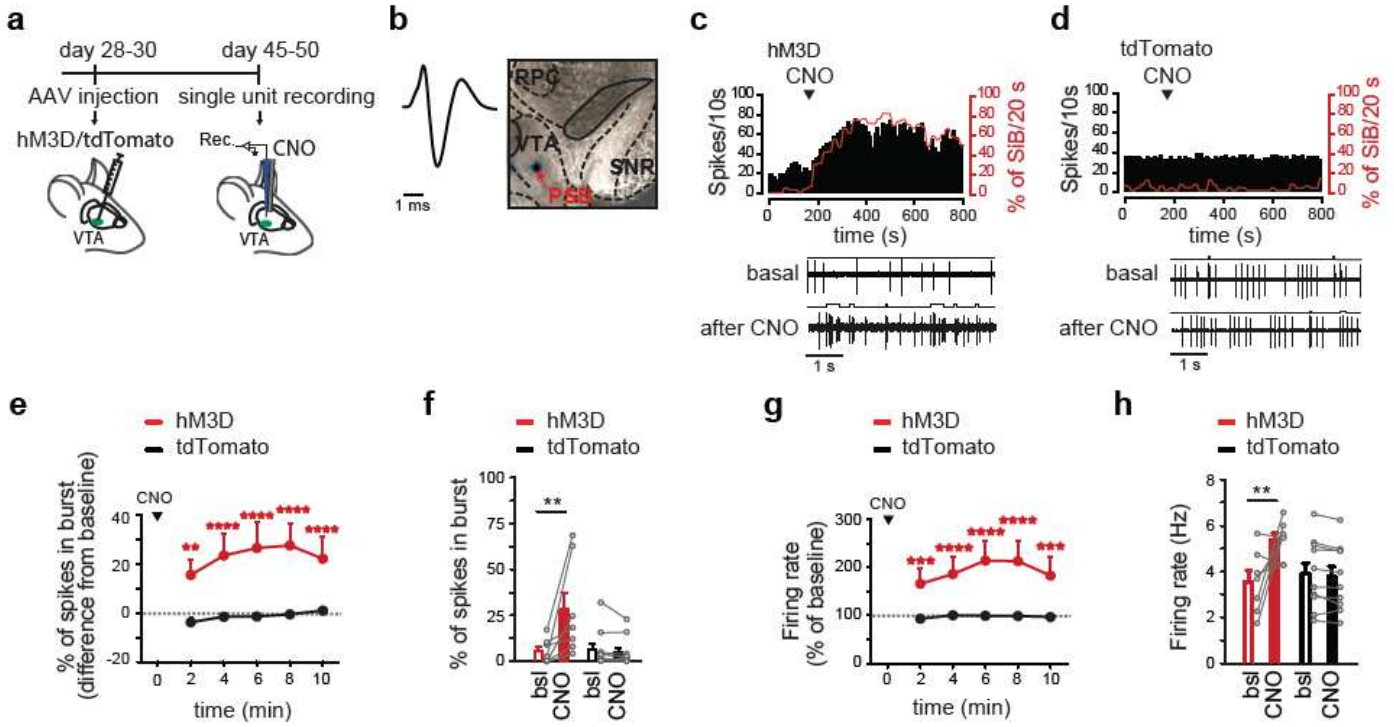

Figure 5

Chemogenetic activation of astrocytes in vivo favors bursting and overall firing activity in VTA DA neurons. a) Schematic of the experimental design showing the pipettes for recording (blue) and CNO application (gray). b) Left, representative action potential (start to end > 2.5 ms) from a putative VTA DA neuron. Right, location of a recorded putative VTA DA neuron. PSB; pontamine sky blue; SNR, susbtantia nigra pars reticulata; RPC, red nucleus. c, d) Upper panels, representative firing rate (Spikes/10 s) histograms and percentage of spikes in burst (SiB/20 s) trends over time of VTA DA neurons from mice expressing hM3D (c) or tdTomato (d) in VTA astrocytes. Lower panel, examples of raw spike traces of the same neurons before and after local CNO applications. e) Time course of the bursting activity (after local CNO applications (hM3D, n = 7; tdTomato n = 10). Two-way RM ANOVA and Bonferroni's multiple comparison test: main effects are not indicated; hM3D 2 minutes vs. hM3D basal **p < 0.01; hM3D 4, 6, 8, 10 minutes vs. hM3D basal **** p < 0.0001. f) Percentage of spikes in bursts before and after local CNO applications (n hM3D = 7; n tdTtomato = 10). Two-way RM ANOVA and Bonferroni's multiple comparison test: main effects are not indicated; hM3D after CNO vs. hM3D basal ** p < 0.01. g) Time course of the firing rate after local CNO applications (hM3D, n = 7; tdTomato, n = 10). Two-way RM ANOVA and Bonferroni's multiple comparison test: main effects are not indicated; hM3D 2, 10 minutes vs.

hM3D basal ***p < 0.001; hM3D 4, 6, 8 minutes vs. hM3D basal **** p < 0.0001. h) Firing rate before and after local CNO applications. Two-way RM ANOVA and Bonferroni's multiple comparison test: main effects are not indicated; hM3D after CNO vs. hM3D basal ** p < 0.01.

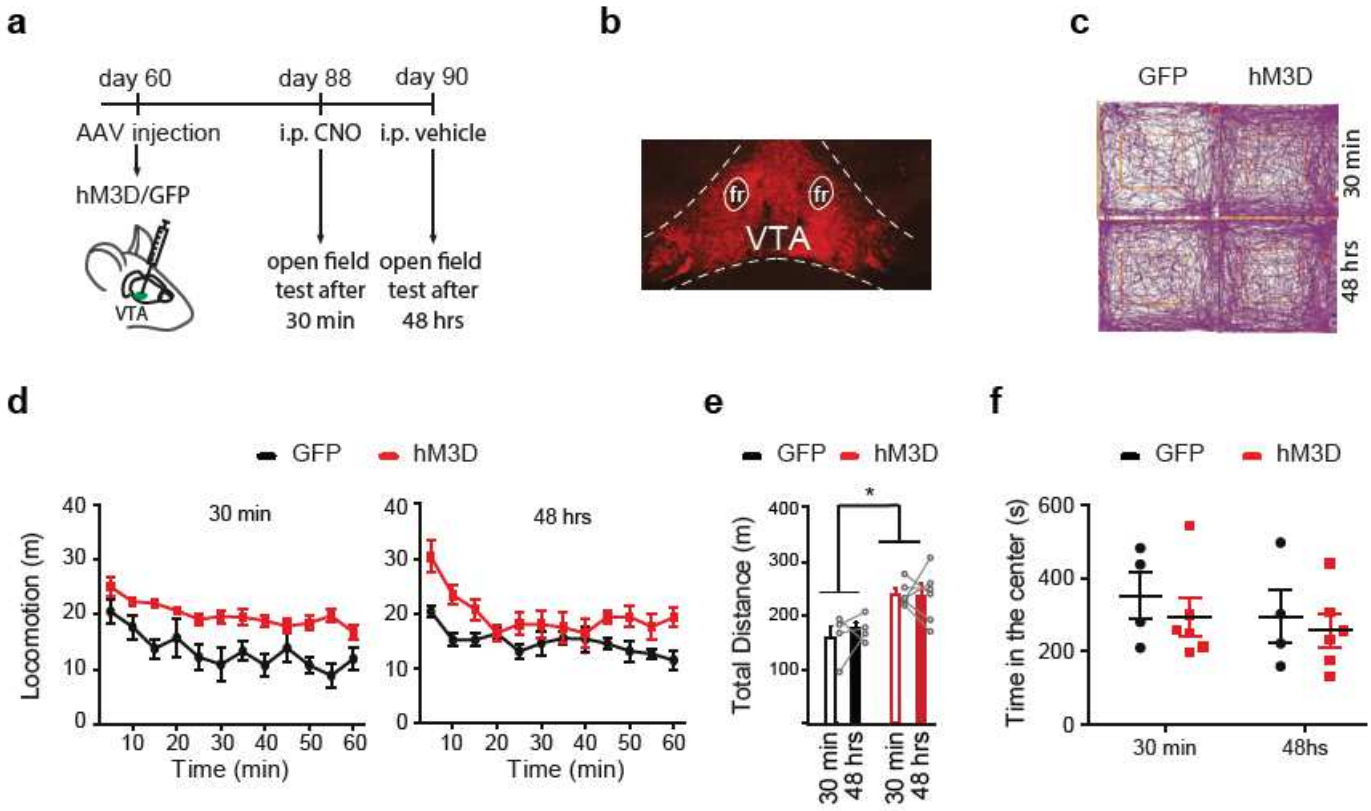

Figure 6

Chemogenetic activation of astrocytes in vivo induces a long-lasting motor hyperactivity. a) Schematic of the experimental design for testing locomotion in mice expressing in VTA astrocytes either GFP or hM3D, 30 min and 48 hrs after the intraperitoneal CNO application (3mg/kg). b) Fluorescence image of hM3D expression in VTA; fr, fasciculus retroflexus. c) Representative examples of locomotion in the open field test. d, e) Locomotor activity (d) and total distance (e) traveled by GFP- and hM3D-injected mice 30 min or 48 hrs after the intraperitoneal CNO injection (3 mg/kg, n = 4-6 mice/group). f) Time spent in the open field center of GFP- and hM3D-injected mice, at different time points after the intraperitoneal CNO injection.

Supplementary Files

This is a list of supplementary files associated with this preprint. Click to download.

- RequieetalSupplementaryinformation.pdf